



EXAMENSARBETE INOM FARKOSTTEKNIK,
AVANCERAD NIVÅ, 30 HP
STOCKHOLM, SVERIGE 2019

Milling accuracy improvement of a 6-axis industrial robot through dynamic analysis

From datasheet to improvement suggestions

PETER ERIKSSON

The thesis had not been possible without the help and support by
the following persons



Professor
Peter Göransson



Master of science
Melanie Gralow

Dipl.-Ing
Georg Cerwenka

*Privatdozent Dr.-Ing.
habil. Dipl.-Ing. Dipl.-Ing.*
Jörg Wollnack



Master of Science (B. Eng.)
Michael Gorn

and finally a special thank you to Ellen Pokorny for a thorough
language and spell check.

Abstract

The industrial robot is a flexible and cheap standard component that can be combined with a milling head to complete low accuracy milling tasks. The future goal for researchers and industry is to increase the milling accuracy, such that it can be introduced to more high value added operations.

The serial build up of an industrial robot bring non-linear compliance and challenges in vibration mitigation due to the member and reducer design. With Additive Manufacturing (AM), the traditional cast aluminum structure could be revised and, therefore, milling accuracy gain could be made possible due to structural changes.

This thesis proposes the structural changes that would improve the milling accuracy for a specific trajectory. To quantify the improvement, first the robot had to be reverse engineered and a kinematic simulation model be built. Next the kinematic simulation process was automated such that multiple input parameters could be varied and a screening conducted that proposed the most profitable change.

It was found that a mass decrease in any member did not affect the milling accuracy and a stiffness increase in the member of the second axis would increase the milling accuracy the most, without changing the design concept. To change the reducer in axis 1 would reduce the mean position error by 7.5 % and the mean rotation error by 4.5 % approximately, but also reduces the maximum speed of the robot. The best structural change would be to introduce two support bearings for axis two and three, which decreased the mean positioning error and rotation error by approximately 8 % and 13 % respectively.

Keywords

Industrial robot, milling, 3D-printing, additive manufacturing, simulation, structural analysis, dynamic modelling, accuracy improvement, configuration screening, simulation automation, HyperWorks

Sammanfattning

En industrirobot är en anpassningsbar och relativt billig standardkomponent. Den kan utrustas med ett fräshuvud för att genomföra fräsoperationer med låg noggrannhet. Det framtida målet för forskare och industri är att öka noggrannheten vid fräsning så att dess användningsområde kan utökas till ändamål som kräver högre precision.

Den seriella uppbyggnaden av en industrirobot medför icke-linjär styvhets- och därmed utmaningar vid vibrationsdämpning. Detta på grund av den strukturella uppbyggnaden då en industrirobot kan förenklat sägas vara uppbyggd av balkelement som i ledpunkterna kopplas samman av växellådor. Med friformsframställning kan en mer komplex struktur erhållas jämfört med traditionellt gjutet aluminiumkonstruktion därmed skulle en ökad noggrannhet vid fräsning kunna uppnås.

Det här examensarbetet föreslår strukturella ändringar som skulle kunna öka noggrannheten vid fräsning för en specifik fräsbara. För att kvantifiera förbättringen, var det först nödvändigt att utgående från tillgänglig data konstruktion en specific robot samt att bygga en kinematisk modell. Därefter automatiserades beräkningsflödet så att ett flertal indata kunde varieras. Detta resulterande i en kombinationsstudie som visade den mest gynsamma strukturella förändringen.

Det visade sig att en minskning av balkelementens massa inte påverkade noggrannheten. Att öka styvheten i balkelementet från den andra axeln skulle dock öka noggrannheten mest utan att behöva ändra robotens uppbyggnad. Att byta växellåda i första axeln kan öka positionsnoggrannheten med nära 7.5 % och rotationsnoggrannheten med cirka 4.5 % men ändringen sänker samtidigt den maximala hastigheten. Den bästa strukturella förändringen vore att introducera ett stödlager vid axel två respektive tre, vilket skulle förbättra positionsnoggrannheten med cirka 8 % och rotationsnoggrannheten med nära 13 %.

Nyckelord

Industrirobot, fräsning, 3D-printing, friformsframställning, simulation, strukturanalys, dynamisk modellering, förbättrad noggrannhet, kombinationsstudie, automatisk simulation, HyperWorks

Contents

1	Introduction	7
1.1	Robotic definitions	9
1.2	Accuracy and repeatability	10
1.3	High value-added operations	11
1.4	Outline	12
2	State of the art	13
2.1	Kinematic analysis	13
2.2	Trajectory planing	15
2.3	Robotic milling	17
2.4	Chatter avoidance	19
3	Problem definition and goals	21
3.1	Method	21
3.2	Delimitation	22
3.3	Goals	22
4	Robotic system description	23
4.1	Specifications	24
4.2	Motor data	25
4.3	Gear ratios	26
4.4	Reducers	27
4.5	Geometry	28
4.6	Kinematic model	29
5	Kinematic simulation	30
5.1	Simulation dataflow	31
6	Static analysis	33
6.1	Pose dependent eigenfrequencies	34
6.2	Optimal milling region	37
6.3	Stability lobe diagram	38
7	Dynamic analysis	42
7.1	Milling trajectory	43
7.2	Milling force	44
7.3	Milling accuracy simulation	46
8	Screening	49
8.1	Structural stiffness increase	50
8.2	Structural mass reduction	52
8.3	Increased gear ratio	53
8.4	Additional support bearing	56
9	Conclusion	58
10	Future work	59

Acronyms

- AM** Additive Manufacturing.
- CMS** Component Mode Synthesis.
- CNC** Computer Numerical Control.
- DDE** Delayed Differential Equation.
- DH** Denavit–Hartenberg.
- DoF** Degrees of Freedom.
- FEM** Finite Element Modeling.
- FRF** Frequency Response Function.
- ITER** International Thermonuclear Experimental Reactor.
- MBD** Multi-Body Dynamics.
- SDm** Semi-Discretization method.
- SLD** Stability Lobe Diagram.
- TCP** Tool Center Point.
- ZOA** Zero Order Approximation.

List of Figures

1	The first industrial robot, the Unimate	7
2	ASEA IRB-60 an industrial robot for spot welding.	8
3	Graphical illustration of bias and variance.	10
4	Typical 5-Axis CNC milling machine.	13
5	LR Mate 200iD 6-Axis robot.	13
6	Denavit-Hartenberg convention.	14
7	Generic Matlab plot of a fifth order polynomial trajectory.	15
8	Down milling direction of motion (Rubeo and Schmitz 2016).	17
9	Regenerative chatter.	18
10	Mode coupling chatter	18
11	SLD method comparison (Cordes et al. 2018).	19
12	SLD experimental validation (Cordes et al. 2018).	20
13	LR Mate 200iD working envelope.	23
14	Robot axes definition.	24
15	LR Mate 200iD internal motor placement.	25
16	Speed-torque characteristics for the GE Fanuc βiSR 0.4 motor model.	25
17	Reducer service illustration for axis 1.	27
18	Corresponding reducer design.	27
19	Exploded view of the robot, illustrating motor and reducer placement within the structure.	28
20	Program interaction within the framework.	30
21	Simulation dataflow.	32
22	1-DoF regenerative chatter model, source: (Panb et al. 2006).	33
23	Point scatter within working envelope.	34
24	First mode shape.	35
25	Eigrl 1	35
26	Second mode shape.	35
27	Eigrl 2	35
28	Third mode shape.	36
29	Eigrl 3	36
30	Fourth mode shape.	36
31	Eigrl 4	36
32	Milling surface data point extraction, to find the optimal region direction, for each point within the working envelope.	37
33	FRF pose and coordinate system definition.	38
34	Real valued FRF in the x-axis direction.	39
35	Real valued FRF in the y-axis direction.	39
36	Real valued FRF in the z-axis direction.	40
37	The stable region in the SLD is below the curve.	41
38	Force validation (Fanuc 2015b).	42
39	Milling trajectories separated in four sides.	43
40	Milling force coordinate axes transformation between local natural and global Cartesian coordinates.	44

41	Periodic milling forces exciting the TCP.	45
42	Nominal error frequency content for side 1.	46
43	Relative position error for the unchanged robot configuration. . . .	47
44	Relative rotation error for the unchanged robot configuration. . . .	48
45	Absolute accuracy due to structural stiffness increase.	50
46	Relative accuracy due to structural stiffness increase.	51
47	Absolute accuracy due to reduced structural mass.	52
48	Relative accuracy due to reduced structural mass.	53
49	Absolute accuracy due to increased gear ratio.	54
50	Relative accuracy due to increased gear ratio.	55
51	Absolute accuracy due to additional support bearing.	56
52	Relative accuracy due to additional support bearing.	57

List of Tables

1	Datasheet specification for each axis.	24
2	Motor specifications.	25
3	Expected reducer gear ratio for each axis.	26
4	Corresponding Harmonic drive reducer specifications.	27
5	Denavit-Hartenberg parameters (Constantin et al. 2015).	29
6	Cutting parameters (Campatelli and Scippa 2012).	40
7	Force and moment output comparison after calibration.	42

1 Introduction

For a long time, automation was practically the same as mechanization, which was one of the fundamental production concepts introduced with the industrial revolution. Repetitive tasks previously carried out by a worker, were replaced by a mechanized processes or a technical device. Mechanization allowed for a single type of product to be mass produced in high volumes, which also meant that production lines became more rigid. Henry Ford and the automotive industry conceptualized the assembly line for mass production and optimized it for high output. Where workers carried out single operations until the end of the line was reached and the product was completely assembled (Karlsson 1991).



Figure 1: The Unimate, a programmable transfer machine and the first industrial robot of its kind (Malone 2011).

The first machine that could replace the repetitive human labor in a production line was installed at General Motors in 1961. The two ton heavy machine seen in Figure 1, was called the Unimate and allowed for die casting and welding of metal parts for an automotive body. It used hydraulic actuators and was controlled by a program stored in a magnetic drum. The Unimate was sold as a programmable transfer machine, developed for "simple" tasks and was developed by the inventor George Devol, together with entrepreneur, Joseph Engelberger (Singh and Sellappan 2013).

The following years, the production and development accelerated and the first robots with sensors appeared in the beginning of the 1970's, along the introduction of the integrated circuit, which meant that computing power became more accessible. The robots developed during this era distinguished themselves from their predecessors by being more aware of their surroundings and included relatively advanced sensory systems (Zamalloa et al. 2017).

In 1973, the German manufacturer KUKA, built the first industrial robot with 6 electro-mechanically driven axes. One year later Cincinnati Milacron, introduced the T3 robot, which was the first commercially available robot con-

trolled by a microcomputer. The Swedish company ABB, released the IRB-6 and its heavier sibling the IRB-60, seen in Figure 2 in 1974 and 1979 respectively. They were the first all-electric and microcomputer-controlled industrial robots which allowed continuous path motion, the fundamental requirement for robotic arc-welding and machining (Nilsson and Pires 2009).



Figure 2: ASEA IRB-60 an industrial robot for spot welding, the heavy weight lifting sibling to the IRB-6 (ABB 1979).

Between the 1970's and 1990's, the industrial robots were equipped, with dedicated controllers, new programming languages, and the ability to be re-programmed. The robot became a natural part of many industries, completing tasks, such as painting, soldering, moving, or assembly.

The robots being developed today, are intelligent robots, delivered with advanced computing capabilities to carry out logical reasoning and to learn by doing. Step by step, artificial intelligence is being introduced, as well as more sophisticated sensors so that the robots can base their actions on more solid and reliable information. Externally, robots have changed color from the warning orange towards more friendly and inviting schemes with the introduction of collaborative robots (Zamalloa et al. 2017).

In automation, robots play a key role and they continue to be introduced in many disciplines. With an ever increasing interest in such systems, the industry is undergoing a transition from mass manufacturing to mass customization. Completely autonomous factories have successfully been built, driven by the trend towards a shorter series of customized products, or products in multiple variants that are not kept in stock, all of which can be offered via the introduction of robots that bring high flexibility and short changeover times (Nilsson and Pires 2009).

1.1 Robotic definitions

The industrial robot comes in various shapes and sizes as well as in number of axes. The number of axes is a physical measure, which typically refers to the number of single Degrees of Freedom (DoF) joints that the manipulator is equipped with. This means that, to reach any point in a plane, a minimum of two axes are required, and to reach a point in space, a minimum of three axes. The combination of the Cartesian position expressed in X, Y, and Z with the orientation composed by rotations around each axis in roll, pitch, and yaw angles, respectively, comprises a full 6 DoF system. Some robots are equipped with even more axes, thus introducing redundant DoFs, in the same way as we humans can move our elbow sideways while holding a glass of water still.

The arrangement of joints and structural members vary depending on the robot type. Common models are the articulated, Cartesian, parallel, delta, or SCARA types (Nilsson and Pires 2009). The robot motion due to a displacement in a joint is dependent on the robot type and is analyzed in the study of robot kinematics. The kinematics chain describes the relationship between the robot motion and a displacement in a joint. From this point on, only articulated robots will be regarded, who are characterized by their serial build up, analogous with the human arm. Each joint is typically equipped with a motor, driving the combined gearbox and bearing called the reducer.

The last link of the robot, at the point where a tool can be attached, is called the end-effector. The kinematic limitations, composes a region in which the end-effector can reach and this region is called the working envelope. Within the working envelope, a certain carrying capacity or payload can be attached to the end-effector, or, essentially, how much weight the robot can lift.

For robots active in both the orientation and rotation domains, the concept of pose is used, which is a location definition for a sub-coordinate system. The sub-system, or simply speaking, the end-effector distance, is defined in Cartesian coordinates, and its inclination in relative angles, both in three dimension. This makes up a 6 DoF transformation, typically used between each joint and computed between the robot origin and the end-effector.

To define the motion of a robot, changes to the joint displacements are applied in the form of rotations. This in turn, causes a movement of the end-effector, as predicted by the kinematic study. Joint-space programming, was originally the way robots were programmed and is still a method used for tasks, such as pick and place. But tasks, such as welding or milling, need defined paths in Cartesian coordinates, which is why the concept work-space programming was introduced. It is a method where a position in the work-space is transformed to the joint-space and can be seen as the inverse of joint-space programming. Work-space programming can however, have more than one solution, analog to holding your arm straight out and either rotating the hand with your shoulder or wrist. The resulting movement of the end-effector, is a geometric path with respect to time, which is the definition of a trajectory. The trajectory can be defined for either the end-effector or rather the tip of the tool attached to the end-effector, called the Tool Center Point (TCP).

1.2 Accuracy and repeatability

There are two types of error measures commonly present in robotics. One of them is the repeatability, which is a measure of how near the robot can return to a previously stored point. In a sense, how close you could focus your arrows on a dart board, which in math terms is called variance, illustrated in Figure 3. The focus of the arrows, does however, not give any information about how far away they are from the actual target, as seen in the left column in Figure 3. This is described by the second error definition, accuracy, analogous to the distance between the cluster of arrows and the bulls eye, or bias, as seen in the right column in Figure 3. The relationship between accuracy and repeatability is approximately a decade (Damak et al. 2005).

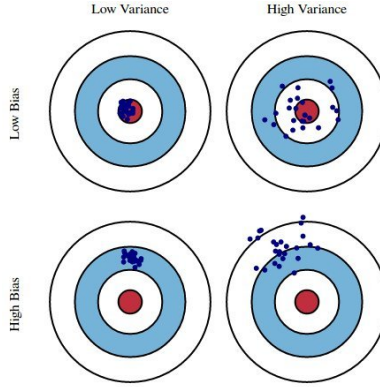


Figure 3: Graphical illustration of bias and variance (Fortmann-Roe 2012).

The repeatability is a good error measure for a lot of robotic tasks, where the actual joint configuration is irrelevant. In this subset of tasks, teaching is a common method of robotic programming, where the robot is moved to a pose and the joint configuration is saved to the memory. This process eliminates the need for the control system to be aware and to compensate for the inaccuracies caused by the mechanical compliance. Simply speaking, when the joint configuration is equal to a saved state, it is assumed that the pose is reached, because the absolute inaccuracies have already been compensated for by the labor teaching the robot.

To reach an unsaved pose in space or to follow a trajectory, the robot has to rely on its accuracy. It is composed by joint transmission and structure compliance, bearing play and the minimum movement due to internal friction. To increase the accuracy, the dynamic properties of the robot have to be improved, which can be accomplished through structural or control performance improvements. The control system can further improve the accuracy from structural optimization with a calibration procedure, normally consisting of four stages: modeling of system, measurement, identification and compensation (Meng and Zhuang 2007).

The accuracy can be increased further by the introduction of a static pose feedback system. A system which is composed by an external measuring device, that feeds the robot control system with an absolute pose of the Tool Center Point (TCP) in real time. The measuring device can be a stereo camera, which have been successfully utilized to reach accuracy levels within the domain of the repeatability (Möller et al. 2016).

1.3 High value-added operations

Introducing the industrial robot into new processes has attracted significant attention from both academics and the industry. Among the fields of research is robotic milling, which has a great economic potential. From an industrial perspective, an estimated 15 % of the value of all mechanical parts manufactured in the world are accomplished by machining operations (Yuan et al. 2018).

As a relatively cheap standard component, with an incomparable flexibility in terms of working envelope and integration, the industrial robot has a lot of potential. To understand, reduce, and compensate structural vibrations, are all big steps towards broad introduction in fields of high value-added operations. Therefore, studies on dynamic robotic vibration analysis are needed, since most of the previous research in the literature were focused on pose accuracy and repeatability (Mousavi et al. 2018). The vibrations occurring during milling affects the quality of the parts, reduces lifetime of tools and deteriorates the robot itself (Mejri et al. 2016).

The industrial robot often has a large mass and a low natural frequency, due to its serial joint configuration. The natural frequency is typically around 10 Hz, compared with several hundred or even 1000 Hz and above for a moving component of a Computer Numerical Control (CNC) machine (Panb et al. 2006). The serial joint configuration is also the reason why an articulated robot has a stiffness less than $1N/\mu m$, whereas a CNC machine often has a stiffness greater than $50N/\mu m$ (Pan and H. Zhang 2007).

New research projects are dependent on the continuous improvements of industrial robots to succeed. The International Thermonuclear Experimental Reactor (ITER) vacuum vessel, is a central component in the fusion power research project. The ITER vacuum vessel needs internal surface finishing through robotic milling, to keep its assembly within the tolerances needed. The current process, is however not accurate enough, which highlights the need for increased accuracy in robotic milling systems (Wu et al. 2014). The same problems restrict the usability of robotic milling of large aerospace parts (Cordes et al. 2018).

Light weight composite materials that replace complicated conventional sheet metal structures are gaining popularity within the transportation industry. The industrial robot as a portable milling operation station, could therefore reduce the need of centralized gantry machines, currently needed for large machining operations. There are examples of mobile milling platforms that have the capability of working in parallel on parts within the production line. The key limitation is, however, still the milling accuracy. (Möller et al. 2016).

1.4 Outline

The contents of the thesis, includes coverage of the state of the art within robotic structural analysis and robotic milling in Section 2. The contribution of this thesis is defined in problem definition and goals in Section 3. The robot system analyzed in this thesis is reverse engineered and described in Section 4. To automate the simulation work flow, a model is described in Section 5. This was necessary due to the many evaluations needed for the static analysis in Section 6 and the dynamic analysis in Section 7. But most of all for the component property variation in the screening done in Section 8.

To summarize, the conclusion suggests the most suitable improvement in Section 9, with respect to the new production capabilities introduced by AM. The outlook of the suggested improvements are discussed in Section 10.

2 State of the art

During the last three decades, industrial robots have undergone a transformation from repetitive and dedicated tools, to highly flexible and reprogrammable manipulators, designed for performance in a variety of tasks. The next step of the research, is to make the industrial robot capable of high value-added applications, such as material removal through milling (Panb et al. 2006).

2.1 Kinematic analysis

To fully understand and predict the end-effector motion, it is crucial to set up an adequate kinematic model. The complexity is dependent on the prediction precision, and the articulated robot is regarded as complicated due to the way in which serial build up introduces modelling challenges. Once completed, the kinematic model can be used for motion planning, to analyze the effect of an introduced change, or for optimization purposes.

A typical CNC machine has its axes aligned with the work-space coordinate system, where an axis displacement is a straight movement in Cartesian space. A movement in Z direction for the CNC machine in Figure 4, is completed by a single linear joint movement. The mechanical properties, in terms of compliance and mass distribution, are approximately equal during the movement.

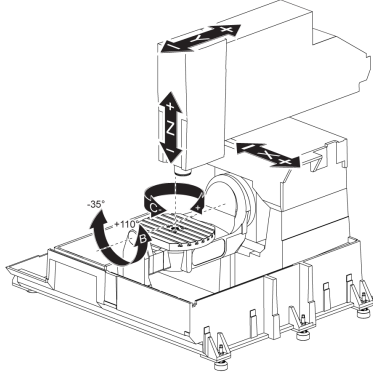


Figure 4: Typical 5-Axis CNC milling machine (HAAS 2012).

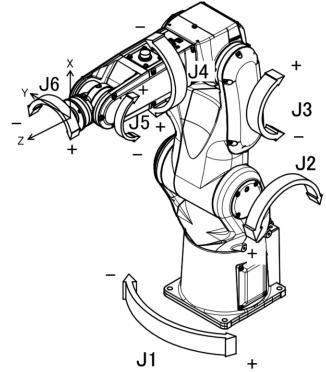


Figure 5: LR Mate 200id 6-Axis robot (Fanuc 2015b).

An articulated industrial robot however, does not possess this property, as a rotation of an axis causes multi-component movements in Cartesian space. The rotation of one axis alters the behavior of every consecutive axis and therefore, industrial robots are said to be kinematic non-linear. The movement in pure Z direction for the robot in Figure 5, is comprised by a synchronized rotary motion in the 2nd, 3rd and 5th axis. During the movement, the compliance and mass distribution is changed, therefore, the articulated industrial robot has a high dynamic, or pose-dependent compliance (Cordes et al. 2018).

Kinematic errors in industrial robots due to compliance and play, are superposed and amplified by the length of each consecutive serial link. The resulting error at the end-effector, is therefore, a large and complex position-dependent compensation problem. Small angle errors in the joints of the robot are caused by manufacturing tolerances in the strain wave gear type of gearbox, as well as alignment errors and gear-tooth interface with frictional losses (Taghirad and Bélanger 1998). The flexing of bearings causes a non-parallel coupling between reducer input and output. This, in turn, causes the end-effector to be out of the plane and dependent on the load of the current pose (Ma et al. 2018).

The assembly of the robots, as well as mechanical wear, introduce kinematic errors in the form of position dependent and periodic kinematic errors. Also the robotic structure, comprised by the traditionally cast aluminum members, adds to the total compliance.

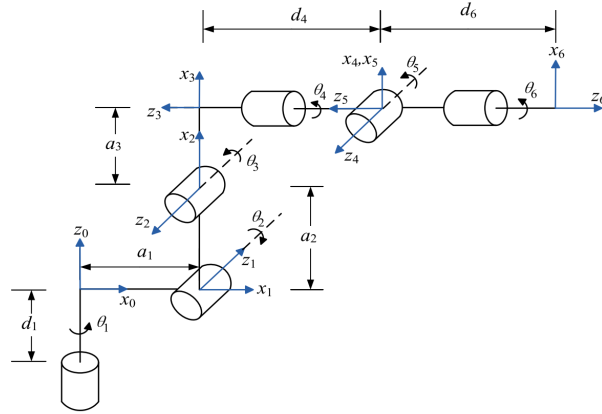


Figure 6: Denavit-Hartenberg convention (Ma et al. 2018).

The conventional way of modelling a robotic system is to describe it as a set of joints and rigid members, illustrated in Figure 6. The convention from Denavit–Hartenberg (DH), is a set of parameters that defines the reference frames for each joint in the kinematic chain. This approach is typically used to model the kinematic behavior due to compliance in joints (Abele et al. 2007; Olabi et al. 2010; Pashkevich et al. 2015), which is motivated by the fact that 50 % to 75 % of the overall compliance, depending on type and robot size, is due to gear compliance (Abele et al. 2007).

To account for the structural compliance with the available CAD geometry of the structure, a flexible Multi-Body Dynamics (MBD) simulation can be done. Simplified beam elements in a Matlab model, were calibrated towards the results of a finite element analysis and subsequently assembled to a robotic system (Mousavi et al. 2018). A static analysis, generated by a finite element model, was used in a MBD to compose a stress measurement of a robot trajectory with respect to kinematic, kinetic, and rigidity (Karagulle et al. 2012).

2.2 Trajectory planning

A manipulator can be programmed to follow an arbitrary path from an initial to a final point in space. The geometrical path becomes a trajectory by the addition of a time law, which includes some kind of constraint, such as duration, maximum velocity, or acceleration for each DoF. The trajectory must be continuous in space, according to fundamental physical laws, meaning that the robot is unable to move between two positions in zero time. Additionally, the trajectory must have a continuous derivative, which otherwise would imply a step in velocity and thus infinite acceleration. The order of continuity or "smoothness" of the trajectory is dependent on the trajectory generation method and "smoothness" reduces the self excited vibrations during motion (Wernholt and Östring 2003).

A trajectory can either be defined in the work-space or in the joint-space. Traditionally, industrial robots are programmed in the joint-space, since many tasks such as pick and place are more or less path independent. This means that the end-effector trajectory is defined by the rotation in the joints. The actual trajectory of the end-effector can be computed with forward kinematics, which is the transformation between joint-space and work-space. The method has advantages of being computationally inexpensive, that the dynamic constraints can be considered, as well as the avoidance of problems with kinematic singularities and axis redundancy (Olabi et al. 2010).

The other option is to define the trajectory in the work-space, which is necessary for machining applications. Planning the trajectories in Cartesian space opens up for direct control of the cutting tool position. This is, however, computationally expensive, since a pose in work-space can have multiple solutions in the joint-space. The inverse kinematics problem must therefore be solved for each interpolated pose in the work-space to find a feasible equivalent in the joint-space within a specified range of accuracy.

To measure the "smoothness" of a trajectory, the concept of jerk has been introduced, which is the derivative of the acceleration. A continuous rate of change of acceleration assures that the applied acceleration is physically representative and that the limitations set by the motor control system can be re-

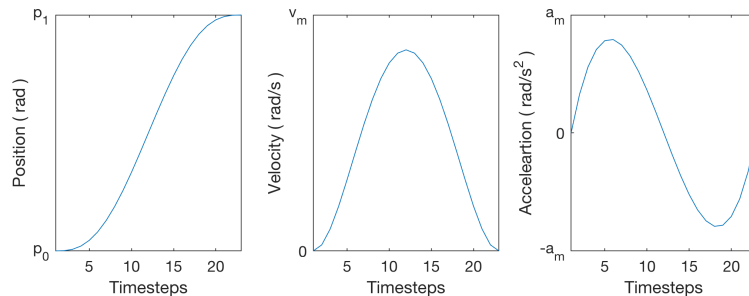


Figure 7: Generic Matlab plot of a fifth order polynomial trajectory.

garded. An arbitrary movement in an axis, from position p_0 to p_1 is illustrated in Figure 7, where the velocity ranges between 0 to v_m and the acceleration varies smoothly between the maximum acceleration applicable, $-a_m$ and a_m .

To minimize jerk or maximize "smoothness", the fifth order polynomial for a trajectory x as a function time t between two points in space is solved. The polynomial coefficients a_0 to a_5

$$x(t) = a_0 + a_1 t + a_2 t^2 + a_3 t^3 + a_4 t^4 + a_5 t^5 \quad (1)$$

can be defined with initial and final constraints, such as position, velocity, and acceleration. The optimum trajectory is analogue to a functional minimum, which is found where its derivative is zero. It was found that the sixth order derivative of the polynomial

$$x(t)^{(6)} = 0 \quad (2)$$

should equal zero to find the smoothest possible trajectory with minimum jerk (Kyriakopoulos 1991).

A smooth trajectory does however, not guarantee a motion without vibrations, since the method only regards rigid kinematic motion. Trajectory pre-compensation is a method where flexible vibrations are predicted during planning and compensated for in the trajectory. This was successfully used to reduce end-effector vibrations with a factor of two, by modeling and predicting the dynamic compliance behavior in a joint. It was accomplished by the selection of a jerk profile, such that the oscillatory behavior of the studied axis was reduced (Oueslati et al. 2012).

When a structural member is subjected to a load, both sides of the natural layer are loaded with strain energy, which in turn causes an elastic deformation. Changes in strain energy causes the member to oscillate, which is nothing less than flexible vibrations. Another way of reducing vibrations was proposed by the definition of a dynamic center, where the amplitude of the vibrations were reduced rather than controlling the oscillatory behavior. The optimization favored a constant deformation, which could reduce the changes in strain energy significantly (W. Zhang 2018).

Vibrations that are excited due to robotic milling can be reduced by the choice of a pose, such that the dynamic stiffness increases. The dynamic stiffness can be altered without effect on the result, since milling is a 5-DoF operation. The rotation axis of the mill is independent off the robot rotation around the same axis. Therefore, optimization with respect to milling axis rotation was investigated and found to be profitable in terms of milling stability and increased material removal rate. The effect of this method was that the trajectory could be optimized during planning in order to reduce the risk of vibrations during milling (Mousavi et al. 2018).

2.3 Robotic milling

Vibrations are more or less present in all machining processes and when left uncontrolled, the vibrations can result in poor surface quality, low productivity, or damage of the tools. Determination of stable cutting conditions is therefore of great industrial interest (Devillez and Dudzinski 2007). The vibrations excited during milling are divided in two main categories: forced vibration and self-excited chatter (Moradi et al. 2008).

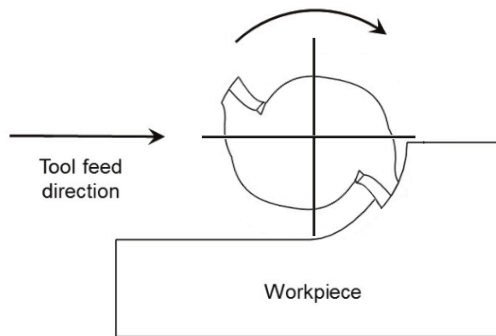


Figure 8: Down milling direction of motion (Rubeo and Schmitz 2016).

The first type can be the clash in Figure 8, between the teeth of the milling tool and the workpiece, causing a time-varying external force that acts on the milling head. The unbalance of a rotary member or a servo motor instability are also examples of forced vibrations. When the unbalance frequency is close to the natural frequency of the robotic system, large vibrations due to resonance are likely to occur (Moradi et al. 2008).

Prediction of the forces that excite the milling head, as the tool tooth cuts through the material, is accomplished by a cutting force model. The forces caused by the cutting motion can be defined analytically and in levels of complexity. The lumped-mechanism model is a cutting force model, which explains the chip breaking force as a cause of friction at the cutting edge of the tool as the tool tooth cuts through the workpiece. The friction is proportional to the chip thickness and by integration along each cutting edge, which is in contact with the workpiece, the cutting forces can be predicted as local forces in the milling tool. These forces can subsequently be transformed to forces acting on the milling head or workpiece respectively (Engin and Altintas 2001).

The second category of vibrations is the self-excited vibrations, which has two mechanisms known as: regeneration and mode coupling. The first chatter mechanism is caused by the repeated cutting of a previously wavy cut surface, resulting in micro-variations of chip thickness that excite the machine structure. The wavy cut surface in Figure 9, illustrates the depth variation of a cut as the tooth cuts through the workpiece. As the chip thickness varies, so does the cutting force, which induces low frequency excitation in the milling head. The

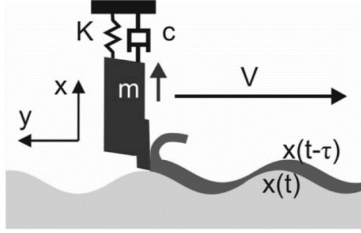


Figure 9: Regenerative chatter (Yuan et al. 2018).

energy comes from the forward motion of the tool and the frequency is typically slightly larger than the eigenfrequency of the lowest flexural mode of the system. This in turn, regenerates a small wave pattern of the surface, which causes regenerative chatter during the next cutting tool pass (Moradi et al. 2008).

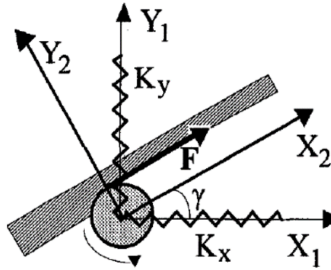


Figure 10: Mode coupling chatter (Yuan et al. 2018).

The second chatter mechanism is mode coupling, which is caused by the relative vibration between tool and workpiece that occurs simultaneously in two different directions in the plane of cut. Mode coupling usually occurs when there is no direct interaction between the milling system and the wavy surface of the workpiece. Therefore, the tool traces out an elliptic path illustrated in Figure 10, as the coupled vibrational modes causes the depth of cut to vary. The chatter frequency is the base frequency of the robot and the spindle speed, width-of-cut, and feed speed do not affect the frequency of chatter (Panb et al. 2006). The amplitudes are practically limited by the non-linearities in the machining process (Moradi et al. 2008).

In the study of CNC machines, it is said that regenerative chatter happens earlier than the mode coupling chatter, and is therefore less of an issue (Moradi et al. 2008). In robotic milling applications, however, the structure stiffness is not significantly higher than process stiffness, which means that they occur in the same frequency range, with mode coupling as the dominant cause of chatter (Panb et al. 2006). The effect of regenerative chatter is vibrations near the cutting tool, whereas mode coupling causes the whole robot to vibrate (Yuan et al. 2018).

2.4 Chatter avoidance

Traditional CNC machines have been studied for a long time and the main cause of chatter in these relatively stiff systems has been addressed to regenerative chatter. In robot milling, however, both regenerative and mode coupling chatter co-exist, and depending on the machining setup, the bottleneck mechanism becomes prevalent. As of now, no single universal chatter suppression strategy exists, which means that the vibration problem has to be solved for each machining configuration and pose (Yuan et al. 2018).

Nonetheless, ways of avoiding chatter in robotic milling exist. To mitigate regenerative chatter, the choice of cutting parameters can be visualized in a Stability Lobe Diagram (SLD), which for a specific machining setup is a representation of the combinations of depth of cut and spindle speed that cause the system to go from stable to unstable. In other words, can the SLD be used to choose a wise combination of milling parameters, such that regenerative chatter is avoided. The prediction data can be inquired experimentally by an impact hammer or by a simulation, both through a Frequency Response Function (FRF) (Altintas and Budak 1995). The SLD must, however, be evaluated for each pose since the industrial robot compliance is pose-dependent and the FRF is a linear combination of the compliance (Cordes et al. 2018).

Vibrations due to regenerative chatter can be modeled by a Delayed Differential Equation (DDE), which accounts for the periodic delay of the rotating machining tool. The Zero Order Approximation (ZOA) is a DDE model that is acceptable for most types of milling processes. Problems can, however, arise when the spindle speed is high and the feed rate low, which is the case for robotic milling. Therefore, ZOA with cross coupling terms of the FRF has been investigated, as well as the Semi-Discretization method (SDm), where Figure 11 illustrates the discrepancies for low spindle speeds (Cordes et al. 2018).

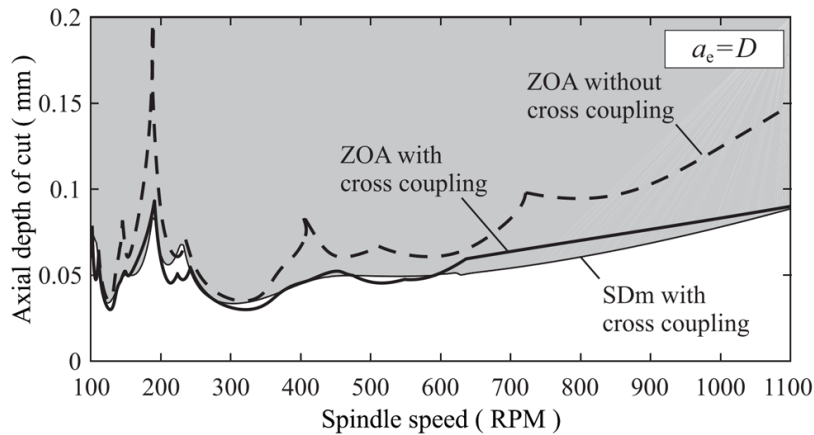


Figure 11: SLD method comparison (Cordes et al. 2018).

There is, however, still no general agreement on which method should be used for generating SLDs for robotic machining process in the research society (Yuan et al. 2018). The ZOA was used with experimental data to generate the SLD for static poses, which proposed that the stability prediction was dependent on the feed direction (Mejri et al. 2016).

The SDm method was experimentally validated in Figure 12 and it was concluded that articulated robots act as high-speed milling machines with the stability dominated by the tool rotation modes. The SDm predicted the stability limits well with relatively high cutting depths despite low structural stiffness. Also no self-excited mode coupling chatter was found at high spindle speeds (Cordes et al. 2018).

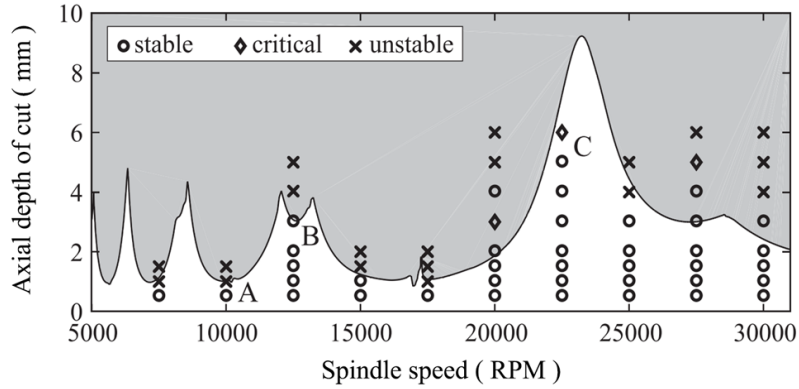


Figure 12: SLD experimental validation (Cordes et al. 2018).

Another way to mitigate regenerative chatter could be to vary the spindle speed dynamically, to accommodate for the wavy surface caused by the previous pass of the cutting tooth. An increase in stability could be reached if speed varying FRF was to be introduced (Grossi et al. 2014)

To reduce the occurrence of mode coupling chatter, either the force must be reduced or the stiffness increased. There are examples of active force control, where the material removal rate is controlled in real time, such that the force exciting mode coupling is not reached. Another approach is to reduce the feed rate and thus also, the cutting force. To increase the stiffness of the articulated robot will mitigate mode coupling chatter. This can be achieved via trajectory planning via functional redundancy or stiffness increase of structural components (Yuan et al. 2018).

3 Problem definition and goals

This thesis will investigate the possible gain of milling accuracy due to design changes in the robotic structure. The robotic milling accuracy will be evaluated for a range of interventions in a screening manner, where each structural change is evaluated separately. The objective is to find the single change that will increase accuracy the most.

With the introduction of Additive Manufacturing (AM), an increase in structural complexity has become viable due to the fact that the manufacturing cost is independent of the part's structural complexity. Therefore, can the typical cast aluminum structure of an industrial robot be revised. The production cost increase of an AM part must, however, be motivated by the increase of milling accuracy.

In the screening procedure, the milling accuracy is defined, in accordance with the proposed dynamic center, as the peak-to-peak vibration amplitude at the TCP. Therefore, will systematic errors or bias not be regarded in favor of reduction of oscillatory movement. The error will be differentiation between position and rotation and rated separately for the following interventions:

- Increased member stiffness.
- Reduced member mass.
- Additional support bearings.
- Increased reducer gear ratio.

The first three interventions, are changes that would be possible to integrate in a part optimized for AM, but the change of reducer gear ratio, which affects the torsional stiffness, will also be investigated. It is a change of a standard component and does, therefore, not pose a change to the structural design.

Reducing mass while keeping the accuracy constant could be interesting with regards to cost savings and possible axis acceleration increase due to reduced second order of inertia. The general purpose of an industrial robot must be regarded and for pick and place a reduced mass would have the positive side effect of lesser inert mass, which could reduce the cycle time.

3.1 Method

To evaluate the milling accuracy, a kinematic model that allows for comparison of structural configurations is needed. The model will be the foundation of the intervention process and once in place, the screening can be conducted. To achieve this, the following tasks are needed:

- Approximation of the robotic system via digital reverse engineering of the Fanuc LR Mate 200iD.
- Finding an appropriate milling surface with the smallest compliance variance in the working-envelope.

- Choosing appropriate cutting parameters such that regenerative chatter vibrations can be neglected.
- Building a simulation model to quantify the vibration error along with a typical milling path.
- Automating the simulation process for an arbitrary number of interventions.

3.2 Delimitation

The field of robotics and milling is enormous; from kinematic analysis to trajectory optimization via control system modelling and structural optimization. To narrow down the span of this work, the following limitations have been regarded:

- No vibrations due to chatter.
- Invariant cutting force amplitude.
- Linear torsional stiffness in reducers.
- No feedback control system.
- Motor and reducer have no inertia nor vibration excitation.
- No bearing compliance or play.
- Internal cables and tubes neglected.

3.3 Goals

The development of a method to simulate the milling accuracy is the practical challenge of this thesis. As the analysis is robot specific, the product of this thesis should be something generic that could be applied to new robots. The model build and evaluation should therefore be accompanied by the following aspects:

- Approximation of the dynamic behavior of a robot.
- Development of a framework for robot geometry setup.
- Full automation of simulation data.
- Milling accuracy comparison to ideal path.
- Modular and extensible code.

4 Robotic system description

The Japanese manufacturer Fanuc promotes the LR Mate 200iD as a compact 6 axes multipurpose robot. It has a load capacity of 7 kg, while having a structural weight of only 25 kg, and has the approximate size and reach of a human arm. The robot is intended for the use in automation processes, such as sorting, material handling, and machine integration.

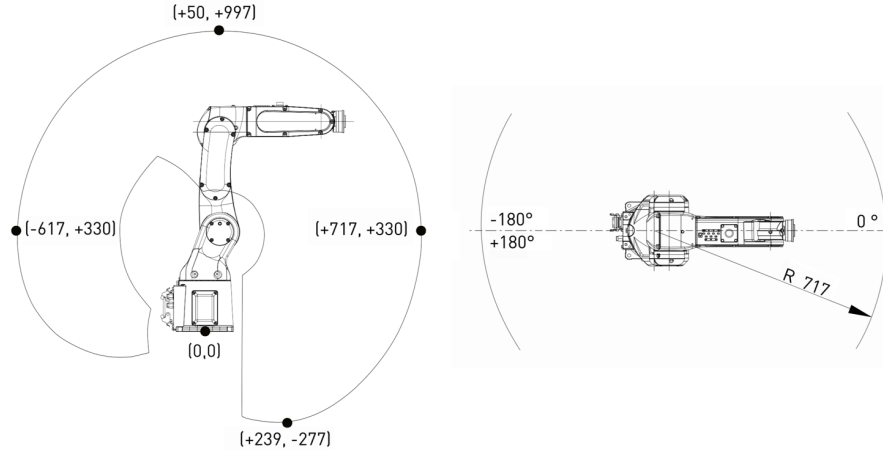


Figure 13: The working envelope, defined for the maximum reach at the rotation center of the fifth axis (Fanuc 2013).

The LR Mate in Figure 13, has a 717 mm maximum extended reach, with a repeatability of $\pm 0.018\text{mm}$ according to the ISO9283 standard. The body is IP67 water and dust protected, while offering integrated signal and air supply from the base to the upper surface of the fourth axis (Fanuc 2013).

No deeper mechanical information could be found about the robot system, which meant that the system needed to be digitally dissected. With the help of the available information, the datasheet, maintenance manual, and operators manual, combined with a surface model of the geometry, an approximated robot was reconstructed.

First, the general system and motor specifications were gathered and combined to obtain an estimated gear ratio. Given the gear ratio, the reducer torsional stiffness could be approximated. Lastly, the surface model had to be solidified and designed.

4.1 Specifications

The Fanuc made robot is an articulated serial robot, which means that each joint carries the weight of the next. Each revolute joint has a specific motion-range, to ensure that the internal cables do not snap nor that the structure intersects with itself.

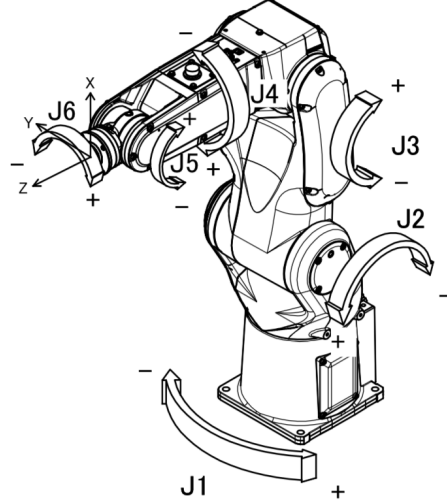


Figure 14: Robot axes definition (Fanuc 2015b).

The three first axes, J1 - J3, compose the translatory motion of the end-effector. Whereas the last three axes, J4 - J6, account for the rotation, which all intersect in the same point at the rotation center of the fifth axis, as seen in Figure 14. This is a common configuration to reduce computational cost during trajectory planning.

Table 1: Datasheet specification for each axis (Fanuc 2013).

Axis	Motion range (deg)	Maximum speed (deg/s)	Load moment (Nm)	Load inertia (kgm ²)
1	360	450	-	-
2	245	380	-	-
3	420	520	-	-
4	380	550	16.6	0.47
5	250	545	16.6	0.47
6	720	1000	9.4	0.15

Partial axis data in Table 1 was missing for axes 1-3. Therefore, the conclusion drawn for axes 4-6 were extended for all axes.

4.2 Motor data

Distributed within the robotic structure in Figure 15 are six servo drive motors, where each motor controls its separate axis. The motors keep track of their absolute position via a built-in encoder and an external control system.



Figure 15: LR Mate 200iD internal motor placement (Fanuc 2015a).

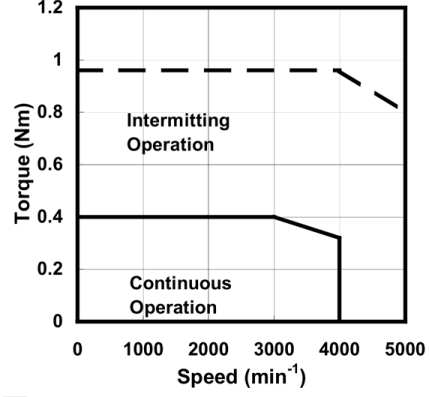


Figure 16: Speed-torque characteristics for the βiSR 0.4 motor model (GE Fanuc Automation 2003).

The high voltage AC motors allow for short-term overloading and maintains almost constant torque up to full speed, illustrated in Figure 16.

Table 2: Motor specifications (Fanuc 2015a; GE Fanuc Automation 2003).

Axis	Model	Stall torque, T_s (Nm)	Speed (RPM)	Brake	Weight (kg)
1	βiSR 1/6000	1.2	6000	•	1.9
2	βiSR 1/6000	1.2	6000	•	1.9
3	βiSR 0.5/6000	0.65	6000	•	1.4
4	βiSR 0.4/6000	0.4	4000	•	1.2
5	βiSR 0.2/6000	0.23	6000		0.33
6	βiSR 0.2/6000	0.23	6000		0.33

The model number for each motor was listed in the maintenance manual, which combined with the servo drive catalogue from Fanuc, was used to obtain, the motor data listed in Table 2. The motors marked with brake have a holding brake to prevent falling along an axis during failure, but they do not decrease the stopping distance during powered deceleration (GE Fanuc Automation 2003).

4.3 Gear ratios

The reducer torsional stiffness between the motor and the structural member is dependent on the gear ratio, the higher the ratio, the stiffer the reducer. Therefore, given the maximum axis rotation speed for each axis $\dot{\omega}_{max}$ (deg/s) and the maximum motor rotation speed n_{max} (RPM), the total gear ratio R_t could be approximated by converting both to (rad/s). This with the assumption that the system was designed for the upper speed limit of the motors and constant torque.

$$\frac{n_{max} \cdot 360}{\dot{\omega}_{max} \cdot 60} = R_t \quad (3)$$

Illustrations of motor and reducer replacement were found in the maintenance manual, which were used to geometrically compare the gear ratio in the first stage between motor and reducer R_m . This was crucial in order to receive the isolated ratio in the reducer R_r .

$$\frac{R_t}{R_m} = R_r \quad (4)$$

The maximum axis load moment, defined in the public datasheet, was used to validate the simplified calculations. The outgoing total torque from the gearbox T_t was calculated by the total gear ratio R_t multiplied with the input motor stall torque T_s from Table 2.

$$R_t \cdot T_s = T_t \quad (5)$$

The total reducer output torque was calculated for each axis, see Table 3 and was used to validate the approximated reducer gear ratio.

Table 3: Expected reducer gear ratio for each axis.

Axis	Gear ratio			Total torque, T_t (Nm)	Torque deviation
	Total, R_t	Motor, R_m	Reducer, R_r		
1	75	1.1	73	96	
2	88	1	95	114	
3	69	1	69	45	
4	65	0.9	48	17	5 %
5	66	1.3	51	15	-8 %
6	36	0.7	51	8	-12 %

Comparing the total torque in Table 3 with the load moment for axes 4-6 in Table 1 showed that a torque deviation within 12 % was achieved with this simple approach. This motivated the extended use of the gear ratio calculations for axes 1-3 as well.

4.4 Reducers

The combined joint and bearing, connecting two structural members with a built-in gearbox, is called a reducer. Its small form factor is made possible by a strain wave gear, which has the advantages of being lightweight with zero backlashes, large gear ratio, high efficiency, and back drivability. These systems suffer, however, from high torsional flexibility, resonance vibration, friction, and structural damping nonlinearities (Taghirad and Bélanger 1998).

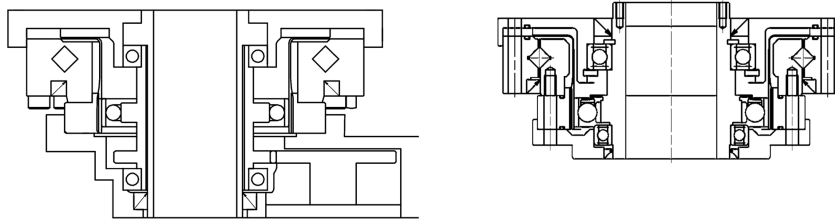


Figure 17: Reducer service illustration for axis 1 (Fanuc 2015b).

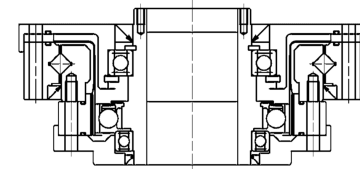


Figure 18: Corresponding reducer design (Harmonic Drive 2018).

No information on the actual reducers used in the robot was available. Only section view drawings as in Figure 17 were available. The German manufacturer Harmonic Drive AG has products that correlate with reducers, that were found in the robot's maintenance manual. This in terms of size, wave dimensions, and gear ratio as seen in Figure 18, are the main variables to the torsional stiffness of the component (Harmonic Drive 2018).

The geometric properties and the gear ratio calculation in Table 3, were used to find near identical sized reducers with most having close to equal gear ratio. The reducer values in Table 4 are the corresponding models from Harmonic Drive for each axis. The mechanical properties of a reducer is, however, complex and often described by a hysteresis torsion curve. Therefore a simplified model with a linear stiffness k_1 and a velocity dependent structural damping can be used (Taghirad and Bélanger 1998).

Table 4: Corresponding Harmonic drive reducer specifications.

Axis	Model	Diameter (mm)	Ratio	Mass (kg)	Stiffness	
					Torsion, k_1 (Nm/rad)	Bending (Nm/rad)
1	SHG-25-2SO	110	80	1.31	$2.5 \cdot 10^4$	$39.2 \cdot 10^4$
2	SHG-25-2SO	110	100	1.31	$3.1 \cdot 10^4$	$39.2 \cdot 10^4$
3	SHG-20-2SO	85	80	0.81	$1.3 \cdot 10^4$	$25.2 \cdot 10^4$
4	SHG-20-2SO	90	50	0.81	$1.3 \cdot 10^4$	$25.2 \cdot 10^4$
5	SHD-17-2SH	80	50	0.42	$0.67 \cdot 10^4$	$12.7 \cdot 10^4$
6	CSD-14-2UH	70	50	0.42	$0.67 \cdot 10^4$	$12.7 \cdot 10^4$

4.5 Geometry

Through instructional sketches in the maintenance manual and an online available surface geometry, a simplified function model was created in the CAD design software SolidWorks. The model in Figure 19 gave information about mass distribution, the second moment of inertia, and motor placement, as well as a geometry for the Finite Element Modeling (FEM) analysis. Defeathering of the surface model was needed for a simpler mesh to be applied.

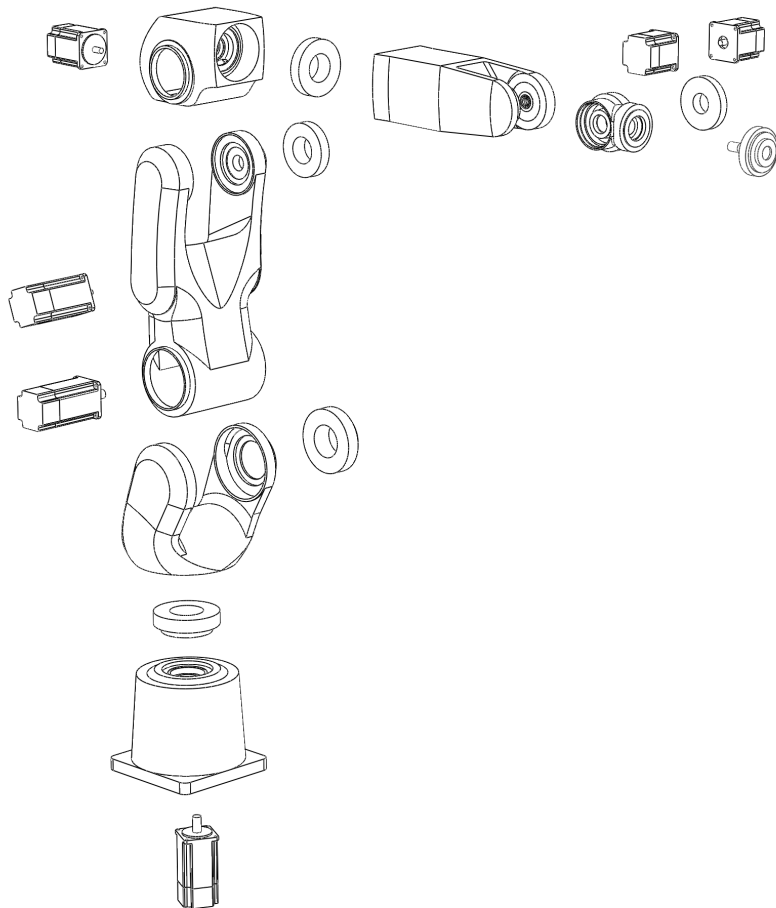


Figure 19: Exploded view of the robot, illustrating motor and reducer placement within the structure.

Due to limited information about the inner geometry of the model, the geometry was only equipped with stiffeners at positions indicated by the maintenance manual sketches.

4.6 Kinematic model

The relation between the motion at the end-effector or TCP and a joint angular displacement is defined by the kinematic model of the robot. Rigid structural members that are connected with revolute joints can be described by the Denavit-Hartenberg (DH) parameter convention. This convention defines the transformation between each joint's local coordinate system and results in a set of matrices that can be multiplied in order to get the transformation between robot base and end-effector or TCP.

Table 5: Denavit-Hartenberg parameters (Constantin et al. 2015).

Axis	θ_i [deg]	d_i [mm]	a_i [mm]	α_i [deg]
1	q1	0	150	-90
2	q2 -90	0	250	180
3	q2 + q3	0	75	-90
4	q4	-290	0	90
5	q5	0	0	-90
6	q6	-80	0	180

With the known DH parameters in table 5, the generation of ideal trajectories was possible through the robotics toolbox in Matlab by Peter Corke (Corke 1995). The toolbox included functions to solve the inverse kinematic problem, to apply Cartesian interpolation and subsequently discretize the trajectory in timesteps.

The trajectories generated by the robotics toolbox used a polynomial interpolation method of 5:th order, to reduce jerk and therefore the self induced vibrations in the robotic structure.

5 Kinematic simulation

It can be practical to write a simulation script that performs the manual labor of setting up the simulation in a FEM software. The benefit of this approach is the total control of the simulation parameters. Another advantage is that once the script is written, it is prepared for a parameter study through the hard coded variables. The script approach thereby simplifies the handling of simulation configurations, thus reduces the risk of input errors.

The screening of possible milling accuracy gain is a multi-parameter study, which introduces a large volume of robot configurations. Depending on the intervention type, listed under the problem and goals section 3, either geometry, joint configuration, or material property is changed. The scripts were, therefore, broken down into modules for each structural component. The modules could subsequently be assembled via a configuration file that allowed for parametric control over all robot component parameters. The modules were structured and unified in a framework manner to ease the integration of new robot models, joint configurations and tools.

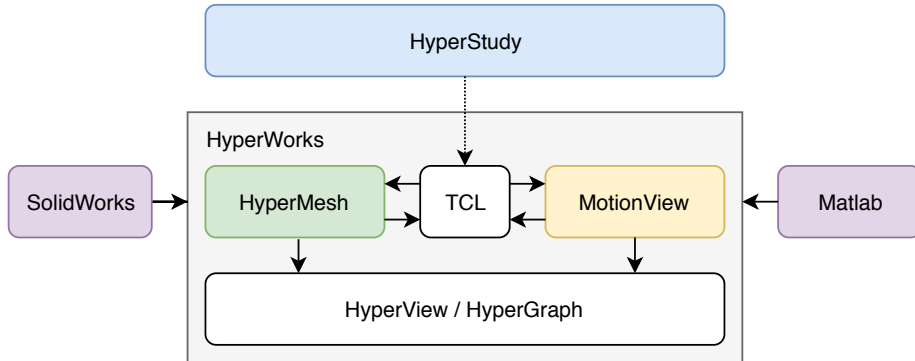


Figure 20: Program interaction within the framework.

The milling accuracy was modeled and quantified with the programs in Figure 20. The programs are stand-alone in the sense that they require manual export and subsequent import to work with each other. Therefore, the built-in scripting language TCL was used to automate the manual labour within the HyperWorks software suite.

To quantify the milling accuracy along the trajectory, the absolute milling position at the TCP was sampled. The sampling was accomplished in MotionView, which is the MBD analysis software within HyperWorks. The Multi-Body Dynamics simulation combines the geometry, trajectory, and milling forces before it executes the simulation and outputs the absolute position of the TCP together with joint displacements and reaction forces. MotionView uses a Component Mode Synthesis (CMS) approach, which requires a pre-analysis of structural members that should be regarded as flexible.

HyperMesh was used to import CAD geometries created in SolidWorks and

subsequently to prepare the members by a pre-analysis. A simplified analysis for the CMS approach that includes compliance, stress concentrations and eigenfrequencies. The structural members were via TCL scripting exported and subsequently imported as flexible components into MotionView. HyperMesh was also used to obtain eigenfrequencies and the FRF for static poses.

To control the robot pose or trajectory, the robotics toolkit by Peter Corke was used. The toolkit is a Matlab toolbox and includes robot kinematics definition, forward and inverse kinematics as well as trajectory planning (Corke 1995). Matlab scripts were written for each trajectory and the results were exported as CSV files. The CSV files were subsequently used in the MBD analysis to control the joint velocity over time. The same approach was used for the static analysis in HyperMesh, with each static pose defined as a set of joint displacements

The program used to setup the screening procedure, was a software specialized in controlling other programs for a user defined model, which is called HyperStudy. It takes a set of input data and applies them to the defined model, which in this case was to run the MBD simulation. This was accomplished by intervening the TCL script controlling the robot assembly in MotionView, thereby granting access for HyperStudy to alter the simulation parameters.

The model was additionally equipped with an export script written in Templex, which is the script language for HyperView and HyperGraph. The script exported the results from MotionView and HyperMesh, via HyperGraph or HyperView depending on the simulation type.

5.1 Simulation dataflow

To obtain the structure change that increases the milling accuracy the most, the Tool Center Point was sampled in a MBD milling simulation. The MBD analysis is a dynamic analysis that need multiple inputs from previous static analysis results as seen in Figure 21. The dynamic milling simulation needs an optimal milling region, cutting parameters from a Stability Lobe Diagram, and pre-analyzed members. The screening parameters controlled by HyperStudy, intervene on the milling simulation parameters and alters member properties on demand, which in turn yields the result of a structural change. The member optimization could be a Topology Optimization, which would need extreme load cases as input, that in turn are dependent on the optimal structural change from the screening. The improvement validation would be the last step where the milling simulation runs with the implemented suggested improvement.

With the mechanical properties approximated in section 4, an optimal milling region could be explored by evaluating the eigenfrequencies within the working envelop. The working envelope was evaluated for a point scatter, where each point corresponded to a pose controlled by HyperStudy. The first four eigenfrequencies were obtained and the region, with the least eigenfrequency variation for all eigenfrequencies combined, was chosen to be the optimum, due to the most equal vibration properties. A milling region with low eigenfrequency variance indicates that the SLD is approximate along the trajectory.

The SLD is pose dependent and uses the result from the optimal milling

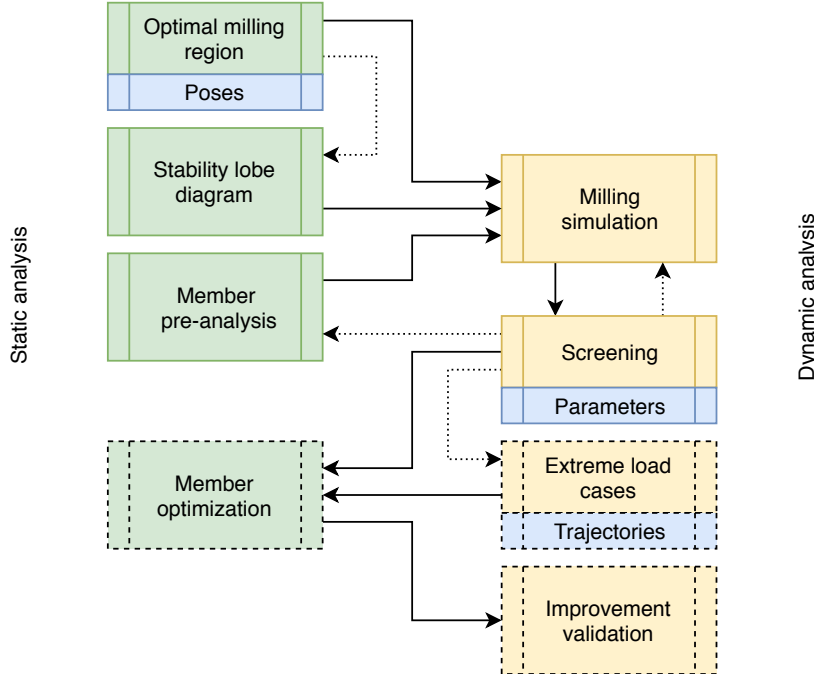


Figure 21: Simulation dataflow where dotted lines are requests and solid lines are returns, whereas dashed boxes represent future work.

region, illustrated in Figure 21, as input. For this pose, a Frequency Response Function was obtained through a static analysis in HyperMesh at the TCP. The SLD was modeled with the ZOA without cross terms, for its simplicity. The simulation does not regard chatter as a source of vibrations and, therefore, only indicative cutting parameters are needed.

In the milling simulation, static pre-analyzed members are needed for components that should be regarded as flexible. The member pre-analysis is on demand and depending on the simulation screening parameters. The generation of flexible members was automated via TCL scripting and was necessary since the CMS approach in MotionView includes the material properties into the results of the pre-analysis. Therefore, must the components pre-analysis be recalculated for each change in parameter, such as geometry, stiffness, or density.

After a first rigid simulation of the robot along the trajectory without any milling forces, the milling simulation is altered by HyperStudy to include the model input parameters. Depending on parameter, members may have to be pre-analysed or the robotic configuration changed to include extra support bearings. Next the flexible robot milling configurations are applied and sampled along the same trajectory with milling forces active and the difference between rigid and flexible configuration is evaluated as the accuracy.

6 Static analysis

The optimal milling region and the cutting parameters are both static results that are needed before the dynamic milling simulation can be executed. The optimal milling region defines where within the working envelope the milling should be carried out, and how the cutting parameters represent cutting depth and spindle speed for a defined feed, material, and milling tool. Stable cutting parameters can be estimated through a Stability Lobe Diagram and thereby avoiding chatter vibrations. The SLD is, however, pose dependent, and therefore needs the optimal milling region as an input.

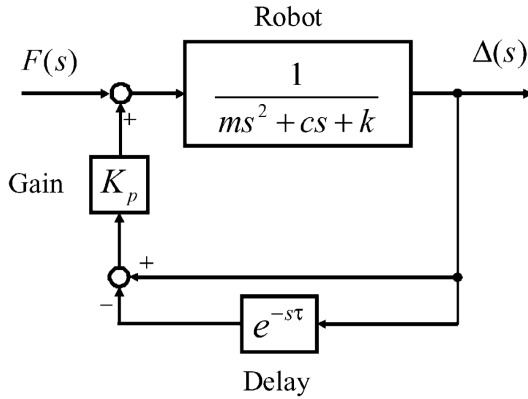


Figure 22: 1-DoF regenerative chatter model, source: (Panb et al. 2006).

The SLD can be modeled by a 1-DoF Delayed Differential Equation, which includes a time delay illustrated in the block diagram in Figure 22. The DDE models the time difference between the cut and the previous cut of the same surface, which is amplified with a certain gain depending on the cutting condition. The simplified model has a diverging output, which is practically limited by non-linearities in the real system. The model transfer function

$$G(s) = \frac{1}{ms^2 + cs + k + K_p(1 - e^{-s\tau})} \quad (6)$$

consists of the three blocks: robotic system, delay, and gain. The robot is represented by a 1-DoF mass-spring-damper system, which is composed by the mass m , viscous damping c , and stiffness k . The cutting conditions are constant, which causes the Gain K_p to be constant whereas the time delay τ is spindle speed dependent (Panb et al. 2006).

The pose dependent parameters m and k also occur in the eigenfrequency equation for a given mode shape, where

$$(\mathbf{K}_x - \omega_{0i}^2 \mathbf{M}_x) \mathbf{p}_i = 0 \quad (7)$$

is a function of M_x , C_x and K_x , which are the robot mass, damping and stiffness matrices in Cartesian space. The natural frequencies and mode shapes of the system are ω_{0i} and p_i respectively (Mousavi et al. 2018).

Comparing equation 6 and 7 indicates that the search for a region, with the most equal SLD would also be the region with the most equal eigenfrequencies, given that the damping in equation 6 is pose-independent. This would imply that the eigenfrequency study could find the optimal milling region where the SLD is valid along the milling trajectory and not only for a specific pose.

6.1 Pose dependent eigenfrequencies

The eigenfrequency for a specific pose within the working envelope is unpredictable due to pose dependent compliance and mass distribution. The working envelope was, therefore, mapped by evaluating the eigenfrequency for a point scatter with 50 mm dispersion in the XZ-plane.

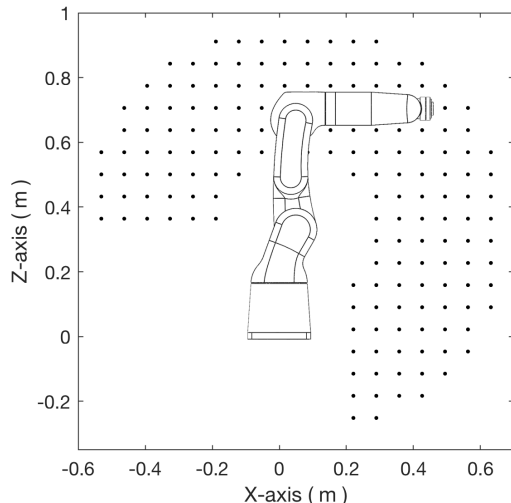


Figure 23: Point scatter within working envelope.

Each point in Figure 23 was transformed to a joint configuration and subsequently, the first four eigenfrequencies were extracted from a static FEM analysis in HyperMesh. For each scatter point, the inverse kinematic problem K^{-1} with respect to the rotation center in the fifth axis, was solved by

$$q_i = K^{-1}(\xi_i) \quad (8)$$

transforming the Cartesian pose ξ_i to the joint-space configuration q_i as joint angular displacements. The resulting list of joint angle configurations were evaluated through a run matrix in HyperStudy.

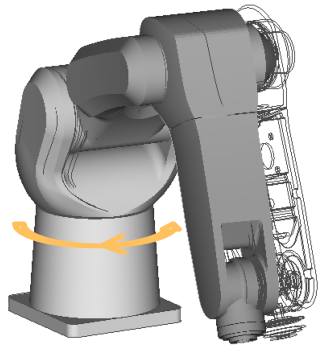


Figure 24: First mode shape, torsion in axis 1.

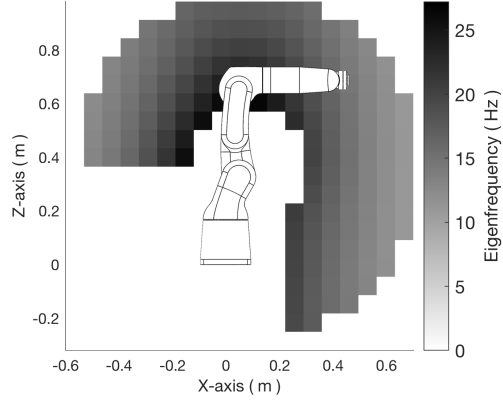


Figure 25: Eigenfrequency response surface for the first mode shape.

The results were subsequently mapped back onto the scatter points and the response surface geometry was plotted for each mode shape respectively.

The response surface geometry is a 3D surface composed by the eigenfrequency for each scatter point and mode shape. The value at each scatter point correlates to a gray scale frequency value, and the surface spanned between four scatter points is a linear gradient between the corner values. The resultant surface is observed as a 2D view, projecting the results onto the XZ-plane, which is the same view as the working envelope from the robot datasheet.

The first mode shape in Figure 24 and the second mode shape in Figure 26 indicates that the reducer torsion and bending stiffness are the major source of

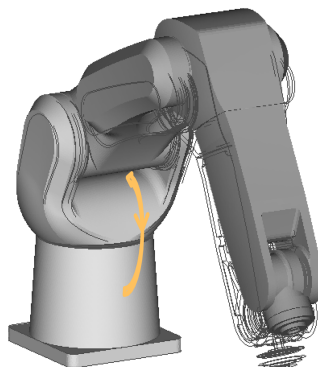


Figure 26: Second mode shape, bending in axis 2.

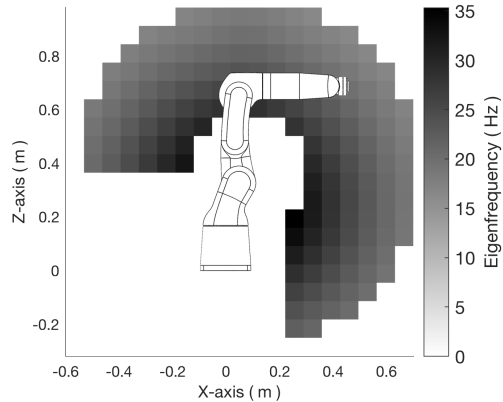


Figure 27: Eigenfrequency response surface for the second mode shape.

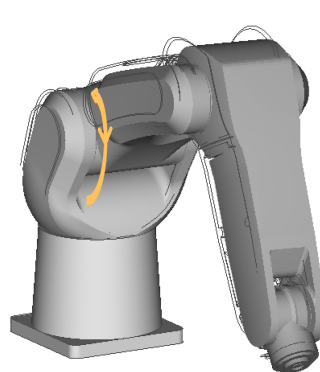


Figure 28: Third mode shape, torsion in axis 2.

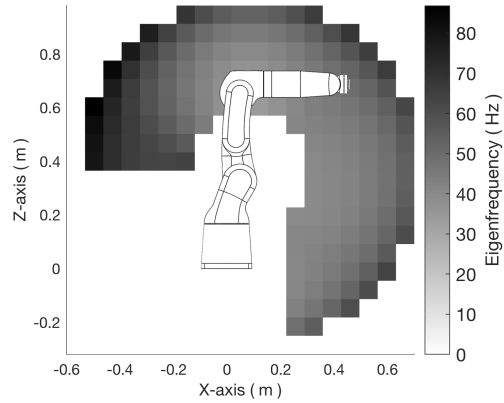


Figure 29: Eigenfrequency response surface for the third mode shape.

compliance. For the first mode the response surface in Figure 25 shows that the eigenfrequency for a tight folded pose is higher than for a pose with great reach. The same applies for the second mode response surface in Figure 27, which seems intuitive.

The inverse behavior in the response surfaces in Figure 29 and 31 are due to pose varying mode shapes. The mode shape varies because of the non-linear compliance, hence the mode shapes in Figure 28 and 30 are only valid near the illustrated pose.

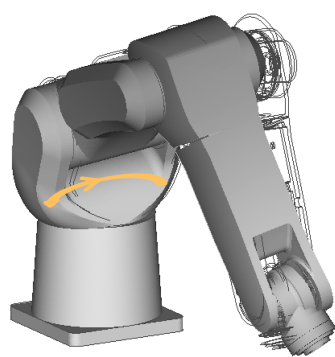


Figure 30: Fourth mode shape, sideways bending in axis 1.

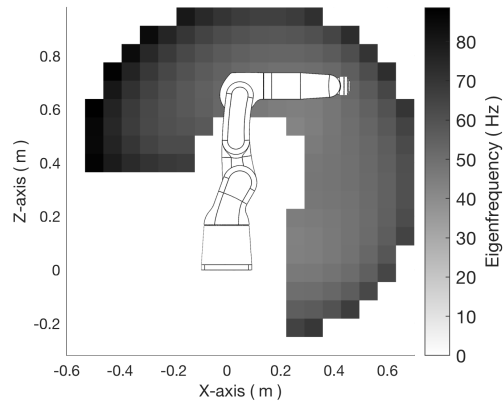


Figure 31: Eigenfrequency response surface for the fourth mode shape.

6.2 Optimal milling region

The results from the eigenfrequency study of the working envelope was used as the input for the search of a region, with a size that contains the milling trajectory, that has the most equal mechanical properties. This milling region should have the lowest peak 2 peak value, for the sum of the four first mode shapes, for it to be called optimal. The trajectory plane or optimal milling region is, therefore, assumed to be the straight line through, four points or a length of 200 mm, where the intersecting points are used as a subset.

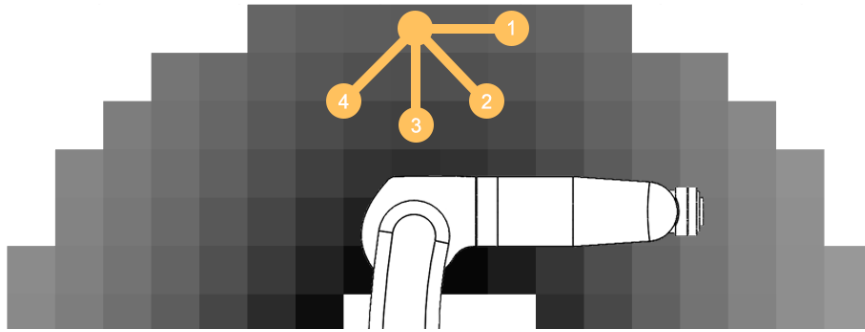


Figure 32: Milling surface data point extraction, to find the optimal region direction, for each point within the working envelope.

The subset starts in the active data point and extends in one of the four directions illustrated in Figure 32. Each data point has, therefore, a peak 2 peak value ω_{p2p} in horizontal, diagonal and vertical direction d that can be summed over the first four modes m via

$$\Sigma_{x_i, z_i, d} = \sum_{m=1}^4 \omega_{p2p} (\omega_{x_i, z_i, m} \rightarrow \omega_{x_e(x_i, d), z_e(z_i, d), m}) \quad (9)$$

the active data point ω has a coordinate index x_i and z_i , which both have their zero point in the top left corner. The peak 2 peak mode sum Σ in Equation 9 was evaluated for subsets with four non-zero data points, with its end points x_e and z_e defined equally as

$$x_e(x_i, d) = x_i + 4 \cdot dir(x, d) \quad (10)$$

where the active data point coordinate index was extended four increments the direction of search. The direction value dir in Equation 10 depending on axis and direction of search matrix in Equation 11.

$$dir = \begin{pmatrix} x & 1 & 2 & 3 & 4 \\ y & 0 & 1 & 1 & 1 \end{pmatrix} \quad (11)$$

The optimum milling region was found to be at $x = 0.49$ m and $z = 0.16 \rightarrow 0.36$ m with a peak 2 peak sum $\Sigma_{17,8,3} = 0.45$ Hz or $\pm 1\%$.

6.3 Stability lobe diagram

Since neither chatter nor mode coupling vibrations were regarded in the kinematic simulation, the purpose of the Stability Lobe Diagram (SLD) was not to avoid vibration mechanisms but rather to find feasible cutting parameters. A chatter free milling path, is dependent on the cutting parameters to lie in the stable region of the SLD. The pose dependent SLD was, however, used to extract the cutting parameters along the complete milling trajectory, since the mechanical properties within the optimal milling region were approximate equal.

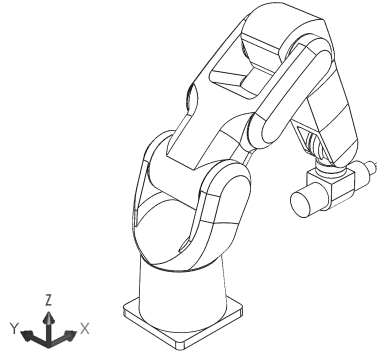


Figure 33: FRF pose and coordinate system definition.

The Zero Order Approximation (ZOA) method of generating a Stability Lobe Diagram is based on the Frequency Response Function. The FRF is normally acquired through the utilization of an impact hammer and the subsequent sampling of an accelerometer. Since no physical robot was available, the data was acquired through simulation in HyperMesh. A unit force was applied at the TCP for the pose in Figure 33 and the frequency range was set to 0 to 2500 Hz. The results were evaluated in the direction of the applied force.

The negative real part lobes of the FRF are searched in the ZOA, since only a negative lobe can yield positive depth of cut a_{lim} . The depth of cut is governed by the equation

$$a_{lim} = \frac{-1}{K_s Z R[H(\omega)]} \quad (12)$$

which includes the combined cutting edge friction K_s , the cutting tool teeth count Z , and the real valued FRF $H(\omega)$. The depth of cut in Equation 12 is given by the ZOA, as well as the combined cutting edge friction via

$$K_s = K_t \sqrt{1 + K_r^2} \quad (13)$$

where the tangential cutting edge friction K_t and the radial cutting edge friction K_r are combined. Values for the cutting edge friction variables in equation 13 are found in table 6.

The data was sampled in a frequency resolution of 0.25 Hz and truncated below 150 Hz, since this region did not contain any negative lobes. The negative lobes were numbered with an axis specific lobe number and a lobe is defined as valid when it crosses the real valued zero from positive to negative and returns positive again. The single lobe in Figure 34 near 1025 Hz has a small value and supports the simplification of the ZOA, where the axial force is neglected and only the in plane forces are concerned (Altintas and Budak 1995).

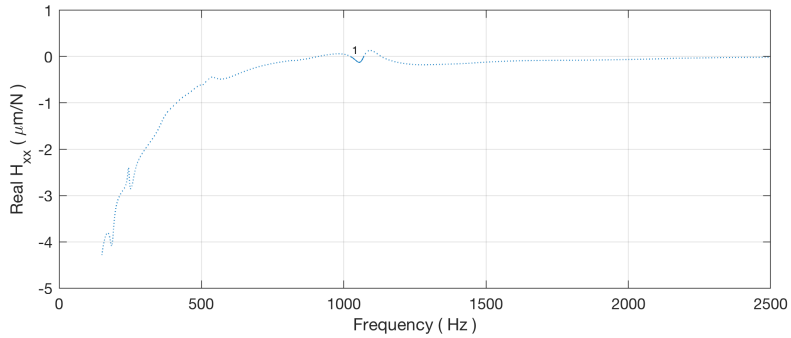


Figure 34: Real valued FRF in the x-axis direction.

The first axis included in the ZOA is the real valued y-axis FRF, with lobes that are an order of 100 times greater than the single x-axis lobe and its compliance directly affects the accuracy of milling. The x-axis compliance affects the depth of cut during milling and is only crucial when facing or slot milling is undertaken. The two negative lobes in the y-axis of Figure 35 are located around 245 Hz and 1030 Hz.

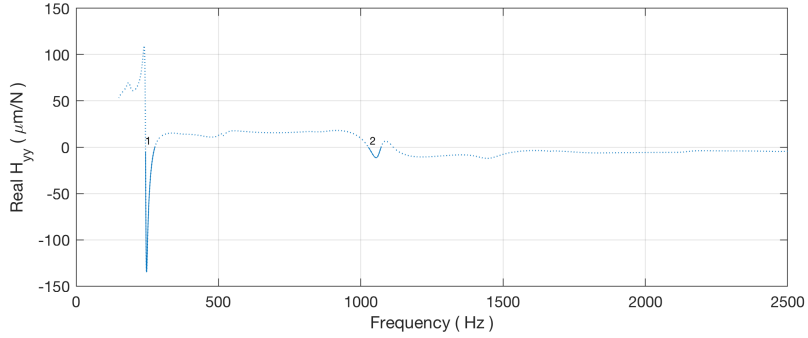


Figure 35: Real valued FRF in the y-axis direction.

The relatively few lobes in the y-axis compared to the z-axis in Figure 36

could be a result of the axes comprising a movement in the unit force direction of the FRF evaluation. The y-axis compliance is mainly due to the torsional stiffness in the reducer of axis 1 and structural flexibility, whereas the z-axis compliance is a combination of the torsional stiffness in the reducers of axes 2 and 3, and structural flexibility.

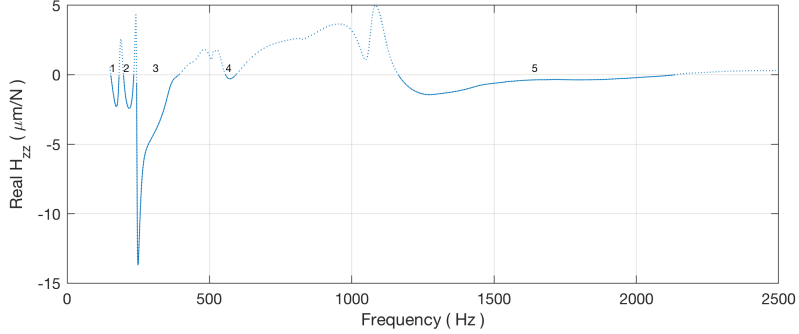


Figure 36: Real valued FRF in the z-axis direction.

The second axis included in the ZOA, is the z-axis, which has real part negative lobes that starts at 153 Hz, 198 Hz, 245 Hz, 556 Hz, and 1165 Hz. The negative lobes can subsequently be converted to a SLD with the introduction of cutting parameters, which are feed, material and cutting tool dependent.

Table 6: Cutting parameters (Campatelli and Scippa 2012).

f_t (mm)	b (mm)	K_{tc} (N/mm ²)	K_{rc} (N/mm ²)	K_{te} (N/mm)	K_{re} (N/mm)	N (RPM)
0.01	1	1780	593	9	7	15000

The cutting properties in Table 6 are for an aluminum alloy 6082-T4 and the cutting tool OSAWA MDCSA2, of 6 mm diameter with two cutting teeth and an helix angle of 42°. The tabulated data and the depth of cut in equation 12 can be combined with the spindle rotation speed n , which is a function of the cutting tool teeth count and the delay time τ , with a factor of 60 to get the unit *RPM*, to generate the transition curve from stable to unstable cutting parameters. The spindle speed equation

$$n = \frac{60}{Z \cdot \tau} = \frac{2\pi \cdot 60 \cdot f_c}{Z(\pi + 2k\pi - 2\phi)} \quad (14)$$

includes the individual lobe number index k , which repeats the lobe and shifts the consecutive lobe down in the frequency domain. The local lobes are placed closer as the number increases and the minimum depth of cut in Figure 37 is equal for each local lobe. The chatter frequency f_c and the phase shift of the eigenvalue ϕ defined as

$$\phi = -\tan^{-1} \left| \frac{I[H(\omega)]}{R[H(\omega)]} \right| \quad (15)$$

The equations 12 and 14 were computed for the negative lobes for both the y-axis and the z-axis. Only the SLD with intersecting lobes are presented since this is a criteria for the SLD to be valid (Mejri et al. 2016).

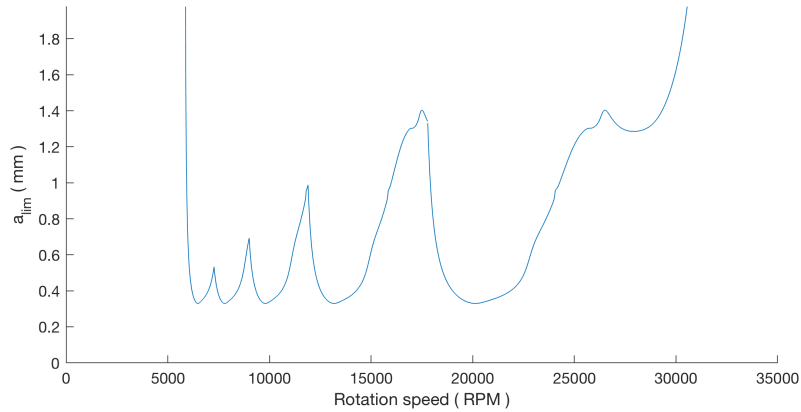


Figure 37: The stable region in the SLD is below the curve.

The Stability Lobe Diagram in the z-axis for the fifth negative lobe number gave intersecting lobes. For 15000 *RPM* the depth of cut was chosen to be 0.5 mm, which is a stable combination according to Figure 37.

7 Dynamic analysis

The kinematic simulation should ideally replicate the behavior of the physical robot, for the results to be plausible, such that proposed changes could increase milling accuracy. To which degree the model represents the reality, could be quantified by the discrepancy in output compared to a known reference scenario. The operator's manual delivered with the robot, stated install structure requirements with maximum forces and moments for specific scenarios and could thus be used as a reference. The forces and moments in Figure 38 act between the robot base and the outer world, where they were quantified during stillness and power-off stop. Two scenarios which represent one static analysis and a set of dynamic analysis. The simulation output could thereby be calibrated in order to minimize static output discrepancies and subsequently be validated.

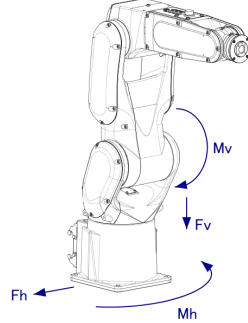


Figure 38: Force validation (Fanuc 2015b).

To calibrate the model, the density of the structure was altered to such degree that the static forces were close to the prescribed force and moment during stillness in the operator's manual. The density was altered since cables, hoses, and the internal design was unknown and, therefore, the uncertainties were assumed to be equally distributed within the robot structure.

Table 7: Force and moment output comparison after calibration.

	M_v [Nm]	F_v [N]	M_h [Nm]	F_h [N]
Stillness	115.5	313.6	0	0
Power-Off stop	768.3	1054.6	402.2	1100.1
Static	116	320	0	0
Axis 1	370	380	406	701
Axis 2	799	789	19	38
Axis 3	337	688	14	30
Axis 2 + 3	928	1104	22	47

The upper part of table 7 are the prescribed values from the operator's manual (Fanuc 2015b) and the lower part of the table contains the simulated values, where the static row translates to stillness and the following rows to the Power-Off stop. All simulated values were obtained with the maximum load capacity of 7 kg at the end-effector and with the acceleration time and axis speed prescribed in the operator's manual.

The actual motions for the Power-Off stop scenario values were not described in the operator's manual and, therefore, were the values assumed to occur with a fully stretched out structure. The isolated rotation in axis 1 and axis 2 yielded a representative moments for the corresponding prescribed values in table 7. An isolated acceleration in axis 3 did not resemble any of the prescribed moments or forces. The combination of maximum acceleration in axis 2 and 3 showed resemblance for the vertical force but an exaggerated moment in vertical axis and was therefore seen as unrealistic.

Approximate static forces and dynamic moments for isolated axes motions were obtained with the density calibrated kinematic model. This indicates that the model yields predictable results for the motions that were foreseeable. No conclusion could be drawn from the simulated forces, since the motion causing the prescribed values were unknown.

7.1 Milling trajectory

The optimal milling region resulted in a slice of the working envelope, where a milling plane could be oriented, such that the mechanical properties were the most equal. A simple square was fitted onto this plane with 200 mm side length as seen in Figure 39. Combining the square path with an fifth order polynomial interpolation method and feed constraints in the robotics toolbox and the milling trajectory could be generated (Corke 1995).

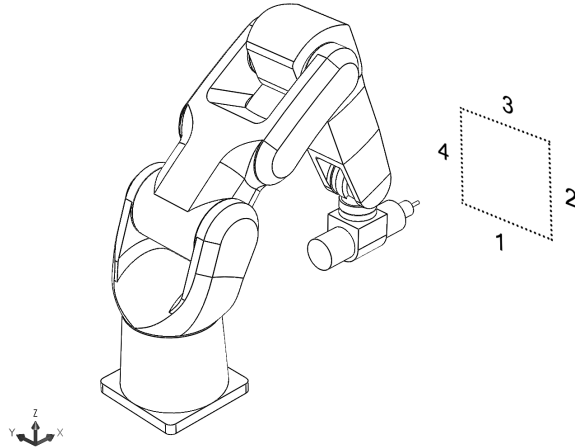


Figure 39: Milling trajectories separated in four sides.

The trajectories were divided into four different sub-trajectories, one for each side, to ease data result separation. Each side was assigned with a maximum chip thickness of $f_t = 0.01 \text{ mm}$, which dictated the feed rate

$$v_{max} = f_t \cdot N \cdot Z \quad (16)$$

The high frequency spindle had a rotation speed of $N = 15000 \text{ RPM}$ and 1.2 kW power, combined with the cutting tool teeth count $Z = 2$ yielded the maximum feed rate $v_{max} = 300 \text{ mm/min}$. The feed rate in equation 16 was set as a constraint in the polynomial interpolation and the velocity at the end points were set to zero. The power of the high frequency spindle was assumed to be of the magnitude, such that the rotation speed could be kept constant during milling.

7.2 Milling force

As the milling tool cuts through material, forces excites the edge of the tool with a period of the rotational frequency of the spindle. The cutting tool forces acts at the TCP and are assumed to be independent of material imperfections along the milling trajectory. Altintas's model was used to evaluate the milling force without considering tool run-out, which is the non ideal properties of drilling, which makes the hole bigger than the drill (Altintas and Budak 1995).

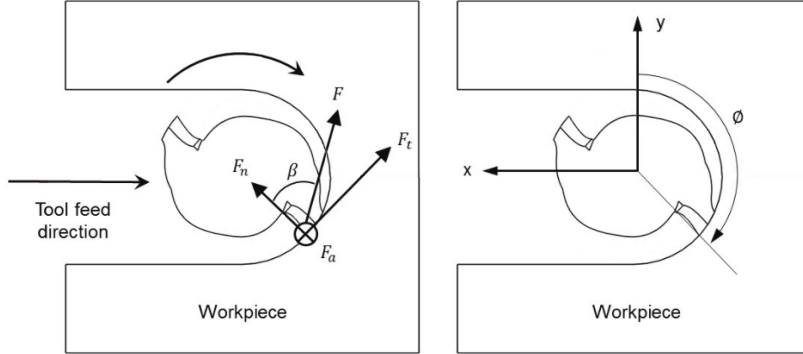


Figure 40: Milling force coordinate axes transformation between local natural and global Cartesian coordinates.

As the milling tool rotates, forces between the tool teeth and the workpiece arises as a consequence of material removal. The local forces acting on the tooth edge, illustrated in Figure 40, are the tangential F_t and normal F_n cutting force components, which are described by the equations

$$F_t = K_{tc} \cdot bh + K_{te} \cdot b \quad (17)$$

$$F_n = K_{nc} \cdot bh + K_{ne} \cdot b \quad (18)$$

where all of the forces are dependent on the chip width b and the chip thickness h . The chip width is the same as the depth of cut a_{lim} determined in Figure 37. The shearing K_c and ploughing K_e force constants that were used are listed in table 6.

As the cutting tool rotates much faster than the movement in the cutting direction, the chip thickness varies as the tool rotates. This is modeled by the Martelloni equation of chip thickness

$$h = f_t \sin(\phi) \quad (19)$$

where the maximum thickness f_t is modulated with a sinusoidal, which is illustrated in Figure 40. For a step movement of f_t in the feed direction, the chip thickness in equation 19 starts at zero and end at zero thickness, with a maximum thickness at the tool rotation angle of $\phi = 90^\circ$.

To convert the local forces at the milling tool to global coordinates and forces acting on the robot TCP, the following transformation matrix was used

$$\begin{bmatrix} F_x \\ F_y \end{bmatrix} = \begin{bmatrix} -\cos(\phi) & -\sin(\phi) \\ \sin(\phi) & -\cos(\phi) \end{bmatrix} \begin{bmatrix} F_t \\ F_n \end{bmatrix} \quad (20)$$

which is given by Altintas's model for cutting forces, which also suggests that the axial force should be neglected. Subsequently the cutting forces, with respect to the tool rotation angle ϕ could be plotted.

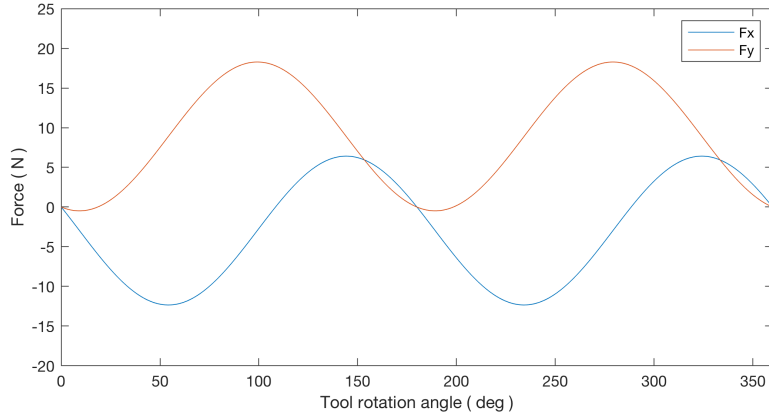


Figure 41: Periodic milling forces exciting the TCP.

Comparing Figure 40 and Figure 41, the force in y-axis direction increases and decreases in x-axis initially, as the first flute cuts through the material surface. The force in the x-axis direction oscillates around zero, since the force direction changes at $\phi = 90^\circ$, whereas the force in y-axis direction is strictly positive with its maximum force at $\phi = 90^\circ$. The y-axis force is maximum at $\phi = 90^\circ$, since the cutting force is proportional to the chip thickness, which is

also the thickest at this tool rotation angle. The cutting forces are periodic with 180° , since the cutting tool has two teeth.

7.3 Milling accuracy simulation

The dynamic simulation of the milling accuracy was done for a rigid and a flexible robot configuration, for the same set of input data. The reason behind two consecutive runs was to get matching data points along the trajectory according to the defined sampling frequency. The relative difference between the configuration's data points for a specific timestamp index $rel_{DoF,i}$ was defined as the unbiased error

$$e_{DoF,i} = rel_{DoF,i} - \frac{1}{n} \cdot \sum_{i=0}^n rel_{DoF,i} \quad (21)$$

relative to the ideal trajectory for each timestep i . The bias compensation term originates from the concept of a dynamic oscillating center where the oscillating amplitude should be minimized (W. Zhang 2018). The term is essentially just the mean value of the sampled data points, differentiated for each DoF.

The error was sampled while the milling force acted at the TCP and the robot followed the milling trajectory side. According to the Nyquist–Shannon sampling theorem the sampling frequency f_s

$$f_s > 2B \quad (22)$$

must be twice the bandwidth B of interest. The spindle rotation speed combined with the cutting tool would demand a minimum of 1000 Hz to fulfill the sampling theorem in equation 22. The sampling rate was, however, set to 100 kHz to capture overtones and to ease generation of figures.

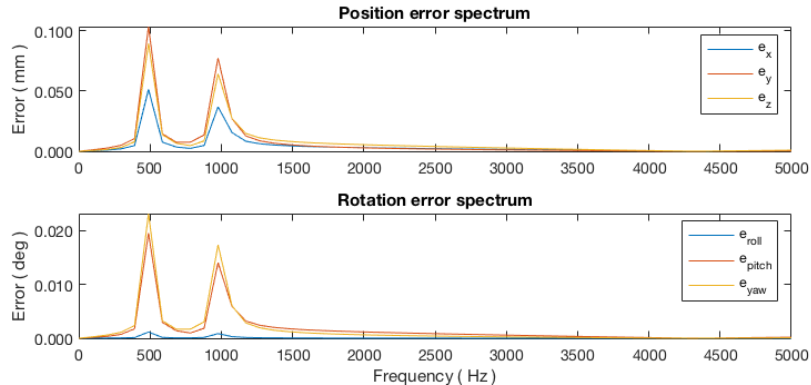


Figure 42: Nominal error frequency content for side 1.

The minimum sampling frequency according to equation 22, would have aliased the second peak in Figure 42, since an overtone of the cutting frequency

was present. The frequency range in the figure was truncated above 5000 Hz, since the upper most interesting peak was the second peak at 1000 Hz. The rotation error around the x-axis e_{roll} was low since the moment required for driving the cutting tool is small compared to the bending moment arising from the cutting forces at the TCP, due to the lever length to the end-effector.

The relative error in equation 21 as a function of the traveled length, illustrates the vibration effects at the TCP in Figure 43 for the position error. The sampled section length was centered around the middle of the milling trajectory side. At this point of the trajectory, the transient effects of applying milling forces and acceleration should be the smallest.

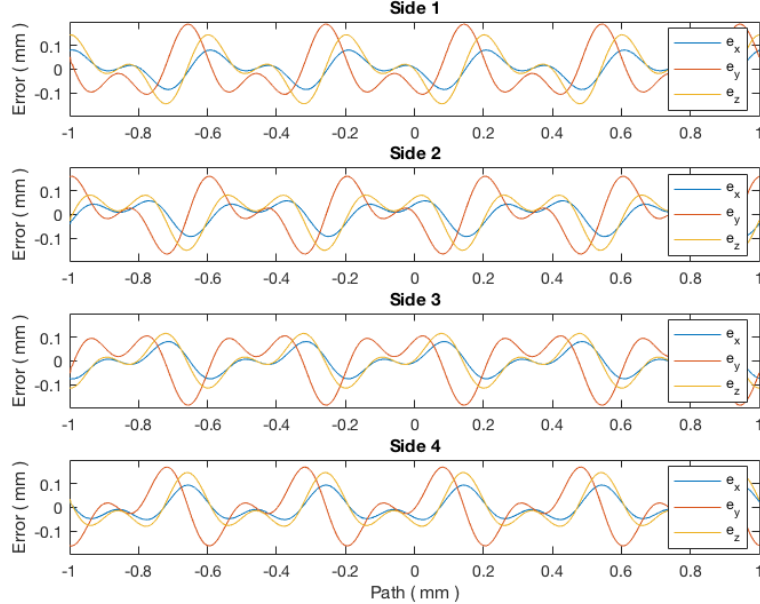


Figure 43: Relative position error for the unchanged robot configuration.

The position error is clearly depending on the milling direction, since the milling force is depending on the side of the milling trajectory square. The x-axis and y-axis force components are depending on the feed direction and, therefore, comparing side one and two in Figure 43, the y-axis e_y and z-axis e_z error switches values and the z-axis roughly becomes the mirrored y-axis error.

Comparing side two and four in Figure 43 shows an inverted profile of the y-axis and z-axis error which also seems intuitive, since they side represent opposite milling directions. The mechanical properties of the system are approximately equal and the sampling occurs along a trajectory that is symmetrical around the YZ-plane and the results are therefore approximately anti-symmetrical as expected.

The rotation error is the unbiased angular displacement of the TCP along the milling trajectory, according to equation 21. The axes are named roll, pitch, and yaw which correlates to the rotation around the x, y, and z-axis respectively. Linear dependency could be expected between some position and rotation error, as a displacement also causes angular displacement, this was however found to be random and therefore the rotational error was regarded as a separate accuracy measure.

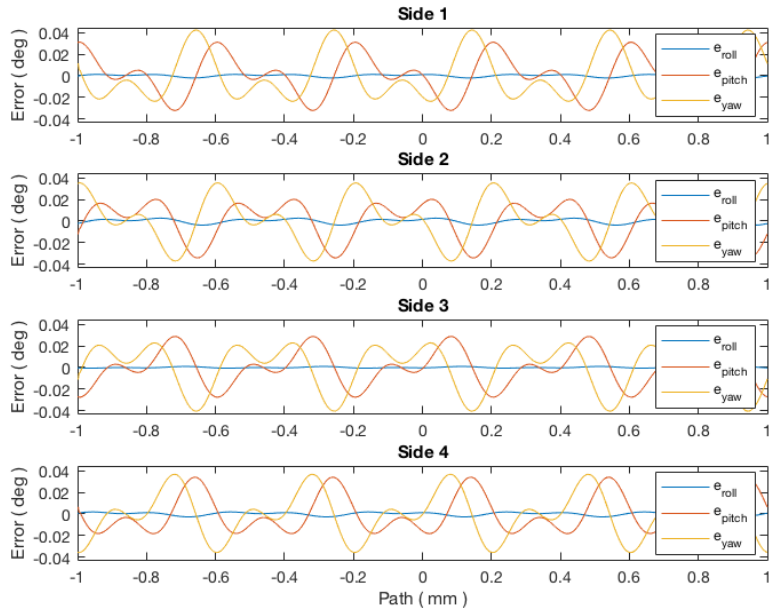


Figure 44: Relative rotation error for the unchanged robot configuration.

The angular error around the x-axis e_{roll} is near zero in Figure 44, which confirms the observation in frequency spectrum in Figure 42. The mirroring effects and the anti-symmetric behavior observed for the position error in Figure 43 is also observed for the rotation error.

The results of the milling accuracy simulation was depending on the damping of the system, which by definition is unknown for a designed system. The structural damping and reducer viscous damping was chosen according to previous external experimental results. The structural members of the robot are cast aluminum parts with a damping ratio set equal to the empirical damping ratio of cast aluminum blocks as 0.0025 (Umashankar et al. 2009). The viscous damping approximation within the reducers were set to 14 Nms/rad, which was the average of experimentally obtain values from various sized robots (Oueslati et al. 2012; S. Zhang et al. 2014; Itoh and Yoshikawa 2003).

8 Screening

The steps up until this point, brought a kinematic simulation model where every parametric value could be altered. The parametric intervention was controlled via HyperStudy and allowed for the possible milling accuracy gain to be investigated by an automated screening procedure. The following parameters were chosen for the screening procedure and the first two were seen as realistically achievable though means of topology optimization:

- Increased member stiffness by 20 %.
- Reduced member density by 20 %.
- Increased reducer gear ratio where possible.
- Additional support bearings where possible.

The input parameters were evaluated isolated, resulting in 23 robot configurations. To inspect the error plots for each DoF separately as a function of distance over the trajectory was not a viable comparison method, as visual inspection and comparison of the result would not be feasible and, therefore, a combined measure for the position DoF and the rotation DoF error was introduced. The positioning error $e_{pos,i}$ was defined as the euclidean distance composed of components from the unbiased error in equation 21 as

$$e_{pos,i} = \sqrt{e_{x,i}^2 + e_{y,i}^2 + e_{z,i}^2} \quad (23)$$

which for each timestep i defines a radius of a fictive error sphere. The error sphere could also be applied to the rotation error even though it represents an angular error, since the rotation error for each component was small

$$\lim_{x \rightarrow 0} \sin(x) = x \quad (24)$$

and could, therefore, be seen as a distance error. With the angular errors treated as distance errors in equation 23, a corresponding rotation error $e_{rot,i}$ combining formula could be composed.

$$e_{rot,i} = \sqrt{e_{roll,i}^2 + e_{pitch,i}^2 + e_{yaw,i}^2} \quad (25)$$

The position error for each timestep was combined into a single valued average error sphere \bar{e}_{pos} , to allow for performance comparison and plotting. The average position error sphere

$$\bar{e}_{pos} = \frac{1}{n} \sum_{i=1}^n e_{pos,i} \quad (26)$$

was computed for each component configuration and side of the trajectory, as the mean value of the position error in equation 23. The average rotation error \bar{e}_{rot} followed analogously

$$\bar{e}_{rot} = \frac{1}{n} \sum_{i=1}^n e_{rot,i} \quad (27)$$

as the mean of the rotation error in equation 25. The output from the screening resulted in a point scatter where the modified configurations were traced and plotted with the configuration number. Each configuration was quantified with a mean rotation error from equation 27 and a mean position error from equation 26. The initial robot configuration is marked with a green dot and the results are displayed in absolute, followed by relative values.

8.1 Structural stiffness increase

When redesigning a part for Additive Manufacturing, the structural stiffness can often be increased while keeping the mass constant. This can be achieved through more complex structures and distribution of mass in shapes not possible to produce through traditional manufacturing. The structural stiffness was increased with 20 % in one part at the time, to probe which part that would benefit the most from a redesign. The part stiffness was altered via the Young's modulus parameter and no regards were taken to implementation.

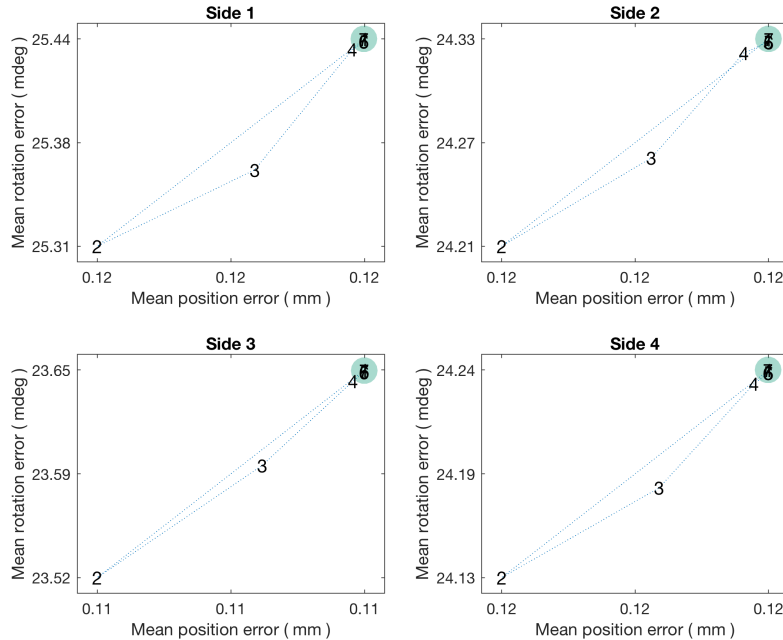


Figure 45: Absolute milling accuracy due to a stiffness increase of 20 %, differentiated for each milling trajectory side.

Each run represents a stiffness increase for a single member and the numbering of the screening result in Figure 45 and Figure 46 have the following interpretation in the robot structure:

- | | |
|------------------|------------------|
| 1. Base | 5. Member axis 4 |
| 2. Member axis 1 | 6. Member axis 5 |
| 3. Member axis 2 | 7. Member axis 6 |
| 4. Member axis 3 | |

The maximum accuracy gain would be obtained if the structural stiffness in the member of axis 1 would be increased. The result is consistent for all four sides of the milling trajectory square. The accuracy gain in Figure 46 is, however, marginal with a maximum position accuracy gain of approximately 1 % and rotation accuracy gain of 0.5 %. The marginal accuracy improvement for most robot configurations was expected since the overall compliance is greatly dictated by the reducers. The accuracy improvement when increasing the stiffness in configuration 2 and 3 is interesting, but could also point out that the digital reverse engineering of the structure geometry was locally poor.

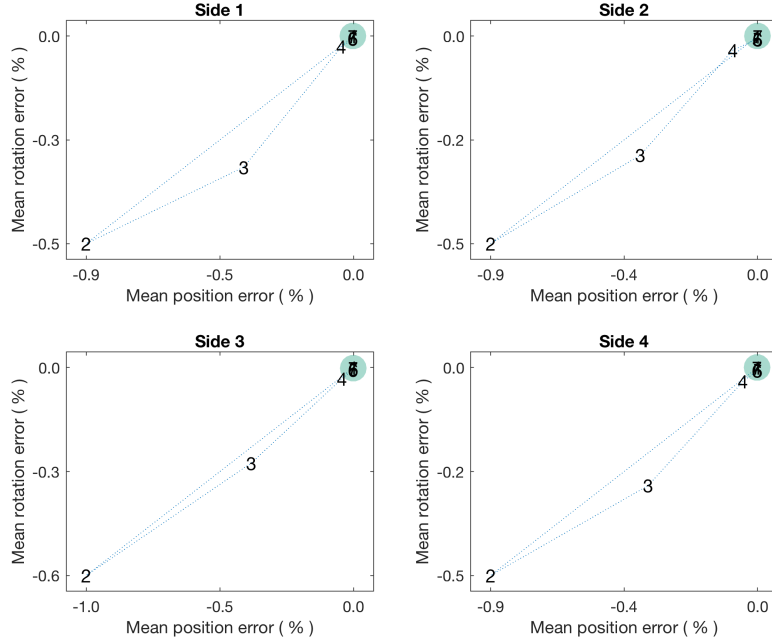


Figure 46: Relative milling accuracy due to a stiffness increase of 20 %, differentiated for each milling trajectory side.

8.2 Structural mass reduction

The objective function during a topology optimization can be set to follow a variety of different responses. The compliance can be minimized with a specific volume fraction or another option is to reduce mass for a constant stiffness. This can be achieved through a change in mass distribution and the resulting geometry can subsequently be accomplished via AM. The mass reduction was altered via the material density parameter of the structure and no regards were taken to how this should be implemented practically.

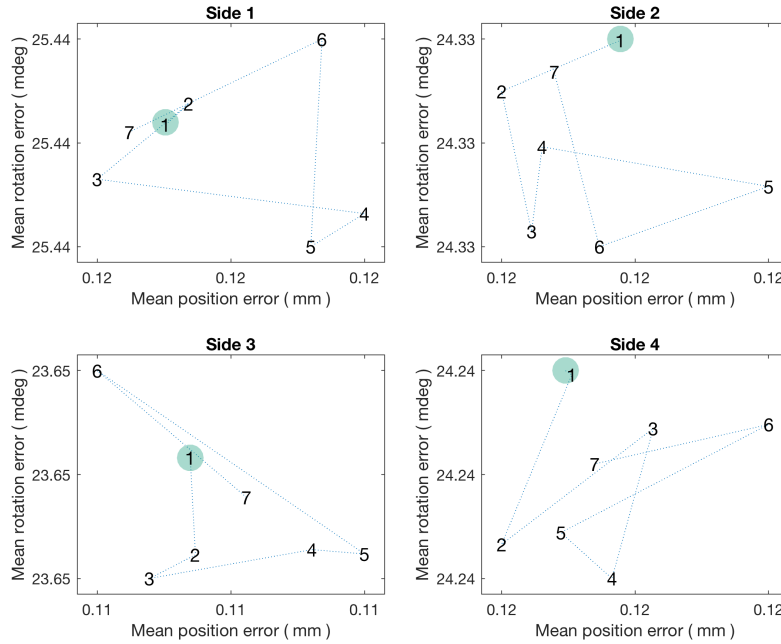


Figure 47: Absolute milling accuracy due to reduced structural mass by 20 %, differentiated for each milling trajectory side.

Each run represents an mass reduction of 20 % for an isolated member and the numbering off the screening result in Figure 47 and Figure 48 have the following interpretation in the robot structure:

- | | |
|---|--|
| <ul style="list-style-type: none"> 1. Base 2. Member axis 1 3. Member axis 2 4. Member axis 3 | <ul style="list-style-type: none"> 5. Member axis 4 6. Member axis 5 7. Member axis 6 |
|---|--|

The decrease of mass in the base member, represented by intervention 1 in Figure 48, did not affect the milling accuracy, which was expected, since the base is a fixed component. The effects of mass decrease in the other structural members are more or less random with negligible accuracy gain.

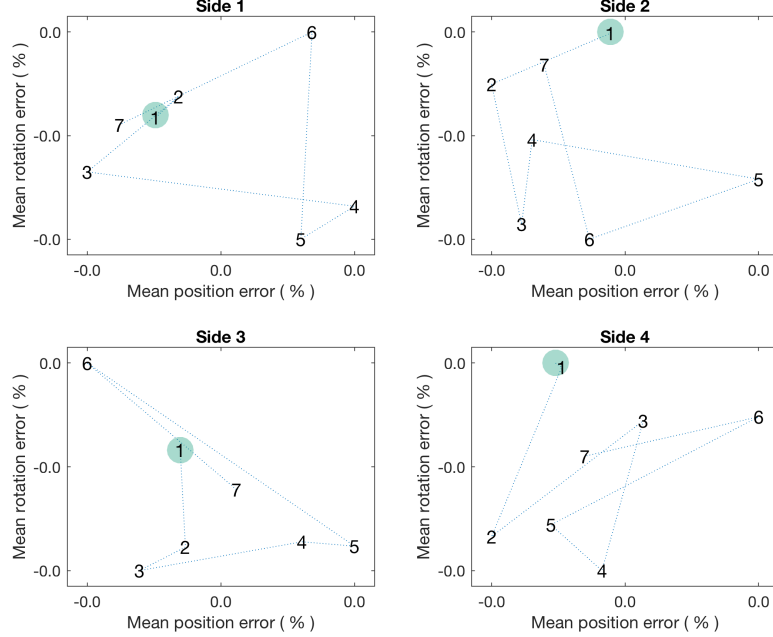


Figure 48: Relative milling accuracy due to reduced structural mass by 20 %, differentiated for each milling trajectory side.

The milling accuracy change due to reduced mass of the structural members affected the mean position and rotation error below the set numerical accuracy of the screening procedure. The observable accuracy improvement in Figure 47 and Figure 48 must not be seen as a discarded alternative but rather a confirmation that the structural mass can be reduced by 20 % in any component with preserved milling accuracy.

8.3 Increased gear ratio

The estimated reducers types within the structure, had versions with the same physical measurements but with a greater gear ratio. An increased gear ratio yields a greater torsional stiffness of the reducer, since more teeth are in connection with each other at given point in time. The trade-off would be a lower maximum speed of the axis, which would not affect the speed of milling. The milling speed is limited by the vibration exciting mechanism due to low stiffness.

The reduced maximum axis speed would probably affect the cycle time during high speed tasks, such as pick and place.

The gear ratio was altered for the axes' that had versions of the reducer with a higher gear ratio and were, therefore, increased to the next possible standard component in the product range from Harmonic Drive. The numbering off the screening result in Figure 49 and Figure 50 corresponds to the following reducers in the robot structure:

- | | |
|-----------|-----------|
| 1. Axis 1 | 4. Axis 5 |
| 2. Axis 3 | 5. Axis 6 |
| 3. Axis 4 | |

Changing reducers in axis 1 or 3 affects the position error as well as the rotation error positively as seen in Figure 49. The results are consistent for all four sides of the trajectory square and the most milling accuracy gain would be obtained if the gear ratio in axis 1 would be increased. The reducer represented by interventions 3, 4, and 5 alters the torsional stiffness of the axes that control the rotation of the robot and the result, therefore, only affects the rotation error.

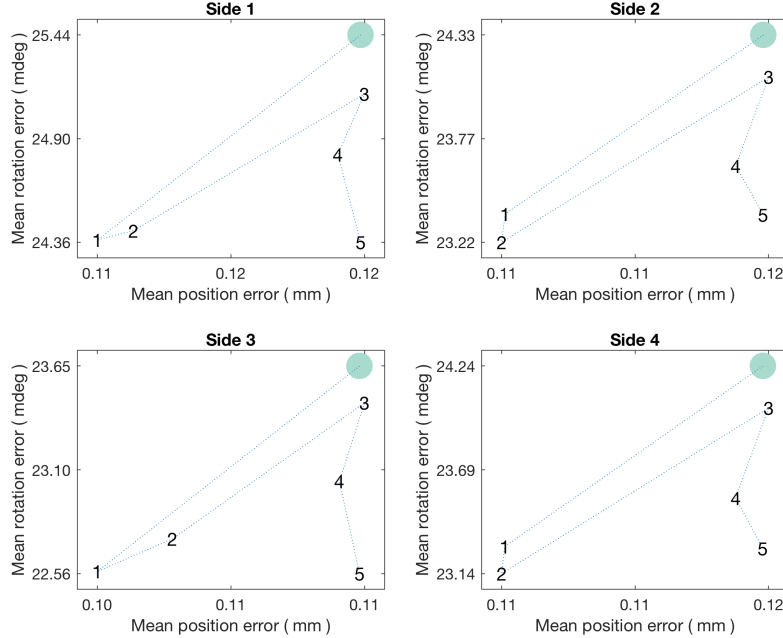


Figure 49: Absolute milling accuracy due to increased reducer gear ratio, differentiated for each milling trajectory side.

An increased torsional stiffness in axis 1 would decrease the compliance in the y-axis milling direction and an increased stiffness in axis 3 would decrease the compliance in the z-axis milling direction, for the approximate pose along the milling trajectory. The increase stiffness in axis 1 or 3 reduces the position error and the rotation error the most since the increase the stiffness in the direction of the applied milling forces.

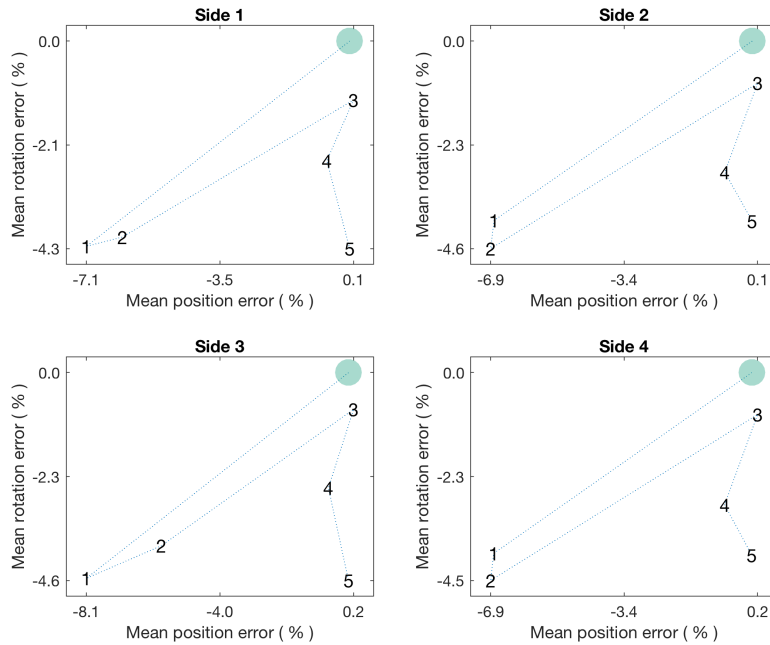


Figure 50: Relative milling accuracy due to increased reducer gear ratio, differentiated for each milling trajectory side.

The mean position error decreased between 6.9 % to 8.1 % and the mean rotation error decreased between 4.3 % to 4.6 % depending on trajectory side, when the gear ratio in the reducer of axis 1 is increased. In absolute values would the increased gear ratio in axis 1 correspond to an increase in milling accuracy of approximately 0.01 mm and 1 mdeg for all sides.

The gear ratio increase in axis 3 would also reduce the mean error in both position and rotation. The accuracy increase depends on the trajectory side more than the increase in axis 1 and performs best on side 2 and 4. The mean position error decreased between 5.7 % to 6.9 % and the mean rotation error decreased between 3.6 % to 4.6 % depending on trajectory side.

8.4 Additional support bearing

The force path through the robotic structure is focused on one side of the robot in axis 2 and 3. This is a design choice to allow simple cable and hose installation through the opposite side of the structure. If additional support bearings were to be introduced, the structural members would be stiffer due to a symmetric force path. The manufacturing of the parts with an integrated support bearing would require increased complexity and could be achieved through optimization for AM. Additional support bearing could only be introduced at two points in the Fanuc LR Mate 200iD structure. The screening configurations investigated if reducers in the following axes could benefit from additional support bearings:

- 1. Axis 2
- 2. Axis 3
- 3. Axis 2 and 3

The milling accuracy gain through the introduction of additional support bearings was consistent for all four sides in Figure 51. Each introduced support bearing decreased the mean position error and the combined configuration of two support bearings show super positioning properties of the isolated solutions.

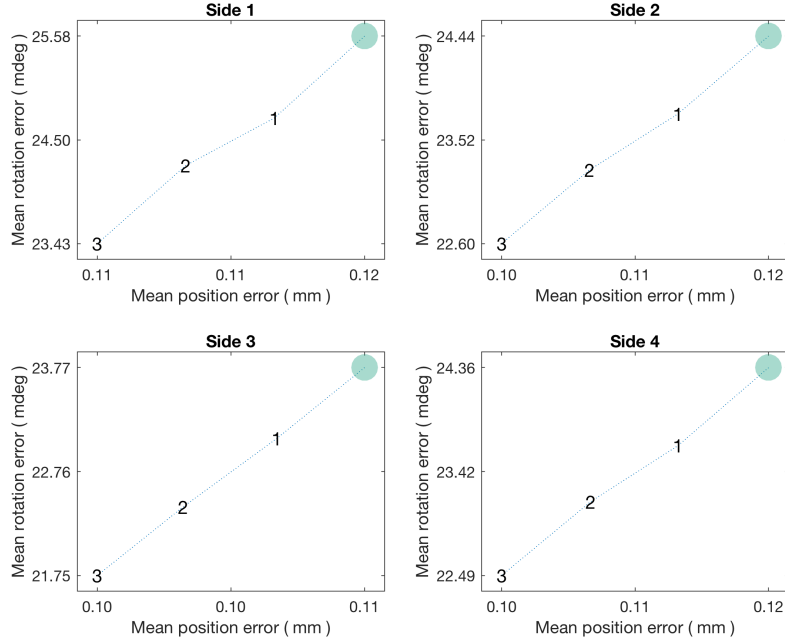


Figure 51: Absolute milling accuracy due to introduced additional support bearing, differentiated for each milling trajectory side.

The relatively large improvement in Figure 51 and Figure 52 could depend on that the reverse engineered structure geometry was defined with a low resolution on the inside. Exaggerated structural compliance due to lack of stiffeners or material thickness could be the case of the performance of the additional bearings. The bending stiffness in the reducers could also be underestimated and an introduced support would therefore give the impression of great improvement.

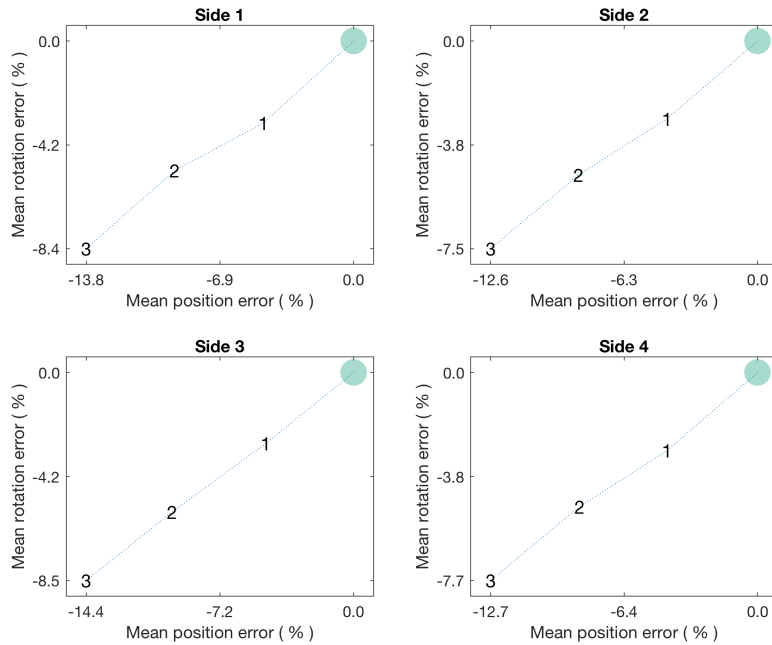


Figure 52: Relative milling accuracy due to introduced additional support bearing, differentiated for each milling trajectory side.

The force path is, however, symmetrical in the case of the support bearings for axis 2 and 3, which would reduce position and rotation errors due to a decreased bending moment in the reducers. The bending stiffness of the structural members near the reducers of axis 2 and 3 is, however, low by design and could therefore benefit from the design proposition and imply that the results from the additional support bearing screening to be representative.

A milling accuracy increase was observed for all configurations, where the best suggestion was to introduce support bearings at both axis 2 and 3. This would according to Figure 52 reduce the mean position error by approximately 13 % and the mean rotation error by approximately 8 %. Further increased in structural stiffness could only be obtained through compliance reduction in the structure members, which was proved marginal effect on the accuracy.

9 Conclusion

This thesis analyzed the milling accuracy improvement potential of an articulated industrial robot from Fanuc called LR Mate 200iD. The progress from datasheet to improvement suggestions was a combination of reverse engineering, robot milling modelling and simulation automation. The milling accuracy was quantified as the error relative around a fictive dynamic center, which only quantified the amplitude of the milling tool regardless of the static error.

In order to address the structural change that should be implemented to improve the milling accuracy the most, a parametric milling simulation model had to be built. To account for the numerous robot configurations, a scripting language was used to automate the simulation steps. This key feature brought an extensive code shell to include every physical property for each component, which opened up for convenient improvement screening.

The inherent low compliance of an articulated industrial robot causes vibration problems not present in conventional CNC machining operations. Therefore, a set of structural properties were varied in order to find where in the robot structure future optimization should be conducted.

An intuitive solution to increase the milling accuracy would be to increase the structural stiffness of the structure. Each structural member was, therefore, individually assigned with a 20 % increased stiffness, which yielded marginal improvement with a maximum position accuracy gain of approximately 1 % and a rotation accuracy gain of 0.5 % for a stiffness increase in the structural member of the first axis. This exposes the fact that the reducers are the weak point of the design and they introduce the majority of the structural compliance.

A structural mass decrease of 20 % was evaluated as an alternative to increasing the stiffness. The results showed that it was possible to implement a mass decrease in every structural member without a measurable milling accuracy difference. This could be profitable for other robotic tasks, such as pick and place and a possible mass decrease would also reduce material cost as well as cycle power consumption.

The weakest link of the system is commonly known, and was also proven, to be the reducers, which have a torsional stiffness that is dependent on the gear ratio. The gear ratio was increased for those reducers that had a corresponding model in the product family from the supplier. It was evident that every increase in gear ratio improved the milling accuracy.

The most profitable change would be the reducer in axis 1, where the mean position error decreased approximately 7.5 % and the mean rotation error decreased approximately 4.5 %. The increased gear ratio would be a simple change of standard component and could be implemented by offering the robot in one slow and one fast version. The only drawback would be the use case where the robot has a mixed operation between milling and demanding pick and place, which is seen as unlikely.

To explore the future design of the human arm sized robot from Fanuc, additional support bearings were introduced in the axis 2 and 3. This could be a viable improvement since the load path of the current design is asymmetric,

which causes bending moment in the axes. An integration of the bearings would be possible if the part design were to be revised and it was shown to reduce the mean position error by approximately 13 % and the mean rotation error by approximately 8 %.

The outcome of the screening procedure suggests multiple design goals for the future optimization of the structure with Additive Manufacturing as a production method in mind. Given the accuracy gain suggested, further amplification could be made possible through control systems design and thereby making AM a viable option for future production of structural members for industrial robots used in milling applications.

10 Future work

With the outcome of the screening, a load case analysis should be conducted to obtain appropriate boundary conditions for a coming optimization. With the boundary conditions available, an optimization in the form of a topology optimization or shape optimization could be performed. This would yield a structural member with improved properties for milling, which should be validated within the kinematic simulation model as a final step.

To increase the accountability of the model choice, the kinematic model developed during this thesis should preferably be calibrated and validated more thoroughly with experimental data from a physical robot. The damping properties of the structure could thereby be incorporated in the model and the pose dependent compliance verified. If no experimental data would be made available, the path of continued simulation could proceed, with improved mapping of the pose dependent compliance. Instead of an eigenfrequency mapping, which is dependent on the mass and the stiffness, a dynamic stiffness analysis should be conducted, in order to find a region with the most equal mechanical properties. The dynamic stiffness would also be a better indicator of the SLD validity.

A conventional robot control software could be used instead of Matlab, to further eliminate causes of error from the simple trajectory planning used. A new model for milling forces should be introduced, since the effective vibrations at the TCP affects the chip thickness. This would cause the cutting force to vary and could therefore model some aspects of chatter.

This could be done if the material surface was modeled as a 2D pixel bed where the cutting edge "cuts" each pixel. A black pixel would describe an uncut surface and a white pixel a cut surface. For each pixel a new milling force should be calculated and as soon as the edge exits the pixel, the force is updated. If the edge enters, a white pixel the force is naturally zero.

References

- ABB (1979). *ASEA IRB 60*.
- Karlsson, Jan M. (1991). “A Decade of Robotics”. In: *Analysis of the Diffusion of Industrial Robots in the 1980s by Countries, Application Areas, Industrial Branches and Types of Robots*.
- Kyriakopoulos, Konstantinos J. (1991). “Minimum jerk trajectory planning for robotic manipulators”. In: *Proceedings of SPIE* 1387, pp. 159–164. ISSN: 0277786X. DOI: 10.1117/12.25421. URL: <http://link.aip.org/link/?PSI/1387/159/1&Agg=doi>.
- Altintas, Y. and E. Budak (1995). “Analytical Prediction of Stability Lobes in Milling”. In: *CIRP Annals - Manufacturing Technology* 44.1, pp. 357–362. ISSN: 17260604. DOI: 10.1016/S0007-8506(07)62342-7.
- Corke, Peter I (1995). “A computer tool for simulation and analysis : the Robotics Toolbox for MATLAB 1 Introduction 2 Representing 3D translation and orientation”. In: *Robotics* 3.1, pp. 24–32. ISSN: 10709932. URL: <http://citeserex.ist.psu.edu/viewdoc/download?doi=10.1.1.26.9656&rep=rep1&type=pdf>.
- Taghirad, H D and P R Bélanger (1998). “Modeling and Parameter Identification of Harmonic Drive Systems”. In: *Journal of Dynamic Systems, Measurement, and Control* 120.4, pp. 439–444. DOI: 10.1115/1.2801484. URL: <http://dx.doi.org/10.1115/1.2801484>.
- Engin, S and Y Altintas (2001). “Mechanics and dynamics of general milling cutters . Part I : helical end mills”. In: 41, pp. 2195–2212.
- GE Fanuc Automation (2003). *AC Servo Motor βis Series Descriptions Manual*.
- Itoh, Masahiko and Hiroshi Yoshikawa (2003). “Vibration Suppression Control for an Articulated Robot : Effects of Model-Based Control Applied to a Waist Axis”. In: 1.3, pp. 263–270.
- Wernholt, Erik and Måns Östring (2003). *Modeling and Control of a Bending Backwards Industrial Robot*. Department of Electrical Engineering Department of Science and Technology. Tech. rep. Linköping: Department of Science and Technology Linköpings universitet.
- Damak, Mohamed, Jérôme Grosbois, and Pierre De Smet (2005). “Vision robot based absolute accuracy measurement, calibration and uncertainty”. In: *Robotics Today (Online Newsletter* March.
- Panb, Zengxi et al. (2006). “Chatter analysis of robotic machining process”. In: *Journal of the Royal Statistical Society. Series C: Applied Statistics* 55.3, pp. 301–316. ISSN: 00359254. DOI: 10.1016/j.jmatprotec.2005.11.033.
- Abele, E., M. Weigold, and S. Rothenbücher (2007). “Modeling and identification of an industrial robot for machining applications”. In: *CIRP Annals - Manufacturing Technology* 56.1, pp. 387–390. ISSN: 17260604. DOI: 10.1016/j.cirp.2007.05.090.
- Devillez, Arnaud and Daniel Dudzinski (2007). “Tool vibration detection with eddy current sensors in machining process and computation of stability lobes using fuzzy classifiers”. In: *Mechanical Systems and Signal Processing* 21.1, pp. 441–456. ISSN: 08883270. DOI: 10.1016/j.ymssp.2005.11.007.

- Meng, Yan and Hanqi Zhuang (2007). "Autonomous robot calibration using vision technology". In: *Robotics and Computer-Integrated Manufacturing* 23.4, pp. 436–446. ISSN: 07365845. DOI: 10.1016/j.rcim.2006.05.002.
- Pan, Zengxi and Hui Zhang (2007). "Analysis and suppression of chatter in robotic machining process". In: *ICCAS 2007 - International Conference on Control, Automation and Systems*, pp. 595–600. DOI: 10.1109/ICCAS.2007.4407093.
- Moradi, H., F. Bakhtiari-Nejad, and M. R. Movahhedy (2008). "Tuneable vibration absorber design to suppress vibrations: An application in boring manufacturing process". In: *Journal of Sound and Vibration* 318.1-2, pp. 93–108. ISSN: 0022460X. DOI: 10.1016/j.jsv.2008.04.001.
- Nilsson, Klas and J Norberto Pires (2009). "Springer handbook of robotics". In: *Choice Reviews Online* 46.06, pp. 46–3272. ISSN: 0009-4978. DOI: 10.5860/CHOICE.46-3272. URL: <http://choicereviews.org/review/10.5860/CHOICE.46-3272>.
- Umashankar, K. S. et al. (2009). "Damping behaviour of cast and sintered aluminium". In: *Journal of Engineering and Applied Sciences* 4.6, pp. 66–71. ISSN: 1816949X.
- Olabi, Adel et al. (2010). "Enhanced trajectory planning for machining with industrial six-axis robots". In: *Proceedings of the IEEE International Conference on Industrial Technology* 18, pp. 500–506. ISSN: 09670661. DOI: 10.1109/ICIT.2010.5472749.
- Malone, Bob (2011). *unimate*. URL: <https://spectrum.ieee.org/automaton/robotics/industrial-robots/george-devol-a-life-devoted-to-invention-and-robots>.
- Campatelli, G and A Scippa (2012). "Prediction of milling cutting force coefficients for Aluminum 6082-T4". In: 1, pp. 563–568.
- Fortmann-Roe, Scott (2012). *Bias and Variance*. URL: <http://scott.fortmann-roe.com/docs/BiasVariance.html>.
- HAAS (2012). *CNC Machine*. URL: <https://www.haascnc.com/service/troubleshooting-and-how-to/how-to/umc-750---service---general-information.html>.
- Karagulle, H. et al. (2012). "Kinematic-kinetic-rigidity evaluation of a six axis robot performing a task". In: *International Journal of Advanced Robotic Systems* 9, pp. 1–9. ISSN: 17298806. DOI: 10.5772/51580.
- Oueslati, Marouene et al. (2012). "Improving the dynamic accuracy of elastic industrial robot joint by algebraic identification approach". In: *ICSCS 2012 - 2012 1st International Conference on Systems and Computer Science*. DOI: 10.1109/IConSCS.2012.6502456.
- Fanuc (2013). *LR Mate 200iD Datasheet*.
- Singh, Balkeshwar and N Sellappan (2013). "Evolution of Industrial Robots and their Applications". In: *International Journal of Emerging Technology and Advanced Engineering* Website: www.ijetae.com ISO Certified Journal 9001.5, pp. 1–6.
- Grossi, N. et al. (2014). "Chatter stability prediction in milling using speed-varying cutting force coefficients". In: *Procedia CIRP* 14.July, pp. 170–175.

- ISSN: 22128271. DOI: 10.1016/j.procir.2014.03.019. URL: <http://dx.doi.org/10.1016/j.procir.2014.03.019>.
- Wu, Huapeng et al. (2014). "Chatter suppression methods of a robot machine for ITER vacuum vessel assembly and maintenance". In: *Fusion Engineering and Design* 89.9-10, pp. 2357–2362. ISSN: 09203796. DOI: 10.1016/j.fusengdes.2014.02.007. URL: <http://dx.doi.org/10.1016/j.fusengdes.2014.02.007>.
- Zhang, Sansan, Si Li, and Wu Wang (2014). "Style for manuscript". In: pp. 2–4. DOI: 10.1007/s11768-014-.
- Constantin, Daniel et al. (2015). "Forward Kinematic Analysis of an Industrial Robot". In: *New Developments in Mechanics and Mechanical Engineering*, pp. 90–95. URL: <http://www.inase.org/library/2015/vienna/bypaper/MECH/MECH-13.pdf>.
- Fanuc (2015a). *LR Mate 200iD Maintenance manual*.
- (2015b). *LR Mate 200iD Operators manual*.
- Pashkevich, a et al. (2015). "Joint stiffness identification of six-revolute industrial serial robots". In: *Robotics and Computer-Integrated Manufacturing* 27.4, pp. 881–888. ISSN: 07365845. DOI: 10.1016/j.rcim.2011.02.003. URL: http://scholar.google.com/scholar?hl=en&btnG=Search&q=intitle:A+Mathematical+Introduction+to+Robotic+Manipulation#0%5Cnhttp://www.ncbi.nlm.nih.gov/entrez/query.fcgi?cmd=Retrieve&db=PubMed&dopt=Citation&list_uids=17241636%5Cnhttp://www.ncbi.nlm.nih.gov/pub.
- Mejri, Seifeddine et al. (2016). "Dynamic characterization of machining robot and stability analysis". In: *International Journal of Advanced Manufacturing Technology* 82.1-4, pp. 351–359. ISSN: 14333015. DOI: 10.1007/s00170-015-7336-3.
- Möller, Christian et al. (2016). "Enhanced absolute accuracy of an industrial milling robot using stereo camera system". In: *Procedia Technology* 26, pp. 389–398. ISSN: 2212-0173. DOI: 10.1016/j.protcy.2016.08.050. URL: <http://dx.doi.org/10.1016/j.protcy.2016.08.050>.
- Rubeo, Mark A. and Tony L. Schmitz (2016). "Milling Force Modeling: A Comparison of Two Approaches". In: *Procedia Manufacturing* 5.January, pp. 90–105. ISSN: 23519789. DOI: 10.1016/j.promfg.2016.08.010. URL: <http://dx.doi.org/10.1016/j.promfg.2016.08.010>.
- Zamalloa, Irati, Risto Kojcev, and Alejandro Hern (2017). "Dissecting Robotics — historical overview and future perspectives". In: pp. 1–9.
- Cordes, Marcel, Wolfgang Hintze, and Yusuf Altintas (2018). "Chatter stability in robotic milling". In: *Robotics and Computer Integrated Manufacturing* 55.July 2018, pp. 11–18. ISSN: 0736-5845. DOI: 10.1016/j.rcim.2018.07.004. URL: <https://doi.org/10.1016/j.rcim.2018.07.004>.
- Harmonic Drive (2018). *Speed Reducers for Precision Motion Control*.
- Ma, Le et al. (2018). "Modeling and calibration of high-order joint-dependent kinematic errors for industrial robots". In: *Robotics and Computer-Integrated Manufacturing* 50.September 2017, pp. 153–167. ISSN: 07365845. DOI: 10.1016/j.rcim.2017.09.006.

- Mousavi, Said et al. (2018). "Stability optimization in robotic milling through the control of functional redundancies". In: *Robotics and Computer-Integrated Manufacturing* 50.July 2017, pp. 181–192. ISSN: 07365845. DOI: 10.1016/j.rcim.2017.09.004. URL: <https://doi.org/10.1016/j.rcim.2017.09.004>.
- Yuan, Lei et al. (2018). "A Review on Chatter in Robotic Machining Process Regarding Both Regenerative and Mode Coupling Mechanism". In: *IEEE/ASME Transactions on Mechatronics* August. ISSN: 10834435. DOI: 10.1109/TMECH.2018.2864652.
- Zhang, Wenxi (2018). "Vibration Avoidance Method for Flexible Robotic Arm Manipulation". In: *Journal of the Franklin Institute* 355.9, pp. 3968–3989. ISSN: 00160032. DOI: 10.1016/j.jfranklin.2018.03.016. URL: <http://linkinghub.elsevier.com/retrieve/pii/S0016003218302205>.

